



HAL
open science

A unified solid/fluid finite element formulation and its possibility for modelling submarine landslides and their consequences

Xue Zhang, Eugenio Oñate, Sergio Andres Galindo Torres, Jeremy Bleyer, Kristian Krabbenhoft

► To cite this version:

Xue Zhang, Eugenio Oñate, Sergio Andres Galindo Torres, Jeremy Bleyer, Kristian Krabbenhoft. A unified solid/fluid finite element formulation and its possibility for modelling submarine landslides and their consequences. *Computer Methods in Applied Mechanics and Engineering*, 2019, 10.1016/j.cma.2018.07.043 . hal-01872683

HAL Id: hal-01872683

<https://enpc.hal.science/hal-01872683v1>

Submitted on 12 Sep 2018

HAL is a multi-disciplinary open access archive for the deposit and dissemination of scientific research documents, whether they are published or not. The documents may come from teaching and research institutions in France or abroad, or from public or private research centers.

L'archive ouverte pluridisciplinaire **HAL**, est destinée au dépôt et à la diffusion de documents scientifiques de niveau recherche, publiés ou non, émanant des établissements d'enseignement et de recherche français ou étrangers, des laboratoires publics ou privés.

1 A unified solid/fluid finite element formulation and its possibility for modelling
2 submarine landslides and their consequences
3

4 Xue Zhang^{1,2*}, Eugenio Oñate², Sergio Andres Galindo Torres¹, Jeremy Bleyer³,
5 and Kristian Krabbenhoft¹
6

- 7 1. Department of Civil Engineering and Industrial Design, University of Liverpool,
8 Liverpool, United Kingdom
9 2. International Centre for Numerical Methods in Engineering (CIMNE), Barcelona,
10 Spain
11 3. Université Paris-Est, Laboratoire Navier, Champs-Sur-Marne, France
12

13 Abstract

14 Consequences of submarine landslides include both their direct impact on offshore
15 infrastructure, such as subsea electric cables and gas/oil pipelines, and their indirect impact
16 via the generated tsunami. The simulation of submarine landslides and their consequences
17 has been a long-standing challenge majorly due to the strong coupling among sliding
18 sediments, seawater and infrastructure as well as the induced extreme material deformation
19 during the complete process. In this paper, we propose a unified finite element formulation
20 for solid and fluid dynamics based on a generalised Hellinger-Reissner variational principle
21 so that the coupling of fluid and solid to be achieved naturally in a monolithic fashion. In
22 order to tackle extreme deformation problems, the resulting formulation is implemented
23 within the framework of the particle finite element method. The correctness and robustness
24 of the proposed unified formulation for single-phase problems (e.g. fluid dynamics problems
25 involving Newtonian/Non-Newtonian flows and solid dynamics problems) as well as for
26 multi-phase problems (e.g. two-phase flows) are verified against benchmarks. Comparisons
27 are carried out against numerical and analytical solutions or experimental data that are
28 available in literatures. Last but not least, the possibility of the proposed approach for
29 modelling submarine landslides and their consequences is demonstrated via a numerical
30 experiment of an underwater slope stability problem. It is shown that the failure and post-
31 failure process of the underwater slope can be predicted in a single simulation with its direct

32 threat to a nearby pipeline and indirect threat by generating tsunami being estimated as well.

33

34 Keywords: Submarine landslide; Unified FE formulation; Monolithic coupling; Fluid-solid

35 Interaction; Mathematical programming; PFEM

36 _____

37 *Email address: xue.zhang2@liverpool.ac.uk

38

39 1. Introduction

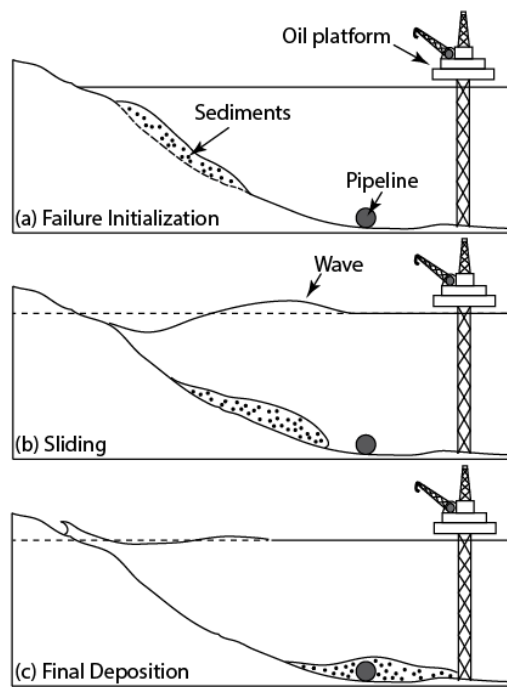
40

41 Submarine landslides are geological phenomena that pose not only a direct threat to offshore
42 infrastructure but also an indirect threat to coastal communities through the generation of
43 tsunamis. Typical examples are the 1998 New Guinea submarine landslide off Papua [1] that
44 caused a tsunami resulting in 2200 deaths and the submarine landslide off Taiwan [2] in 2006
45 that broke seven out of nine undersea cables leading to a major disruption of the internet
46 connection and general commerce between Thailand, Malaysia, Vietnam, South Korea, China
47 and Singapore. In the past decade, submarine landslides have been receiving increasing
48 attention which, to a large extent, due to a boom in offshore infrastructures such as submarine
49 gas and oil pipelines, offshore wind farm and electricity grid infrastructure, deep-water oil
50 and gas platforms etc.

51

52 The timely forecast of a potential submarine landslide, as well as a realistic estimation of its
53 post-failure behaviour and consequences, is undoubtedly of great significance for minimising
54 the degree of destruction. Conventional geotechnical approaches, such as the limit
55 equilibrium method, the limit analysis method and the displacement-based finite element
56 method that are widely used for slope stability analysis normally stop at the point when

57 failure is triggered and do not provide information regarding the post-failure process. To
58 forecast a submarine landslide and estimate its potential impacts, ideally the complete process
59 of submarine landslides ranging from its failure initiation through migration to its final
60 deposition is produced via a single simulation seamlessly. This task however is formidable
61 due to the complex coupling mechanism involved in the process as well as the solid-fluid
62 transitional behaviour of the evoked submarine soil mass.



63

64

Figure 1 Submarine landslides and their consequences.

65

66 In a submarine landslide, the sediment behaves like a solid before the slide is initiated (Figure
67 1(a)) and after the sliding mass eventually comes to rest at a new location (Figure 1(c)), but
68 mimics a fluid during the sliding process (Figure 1(b)). When the post-failure stage is
69 concerned, the sliding sediment is commonly simulated based on the framework of fluid
70 mechanics, due to its fluid-like behaviour. In the simulation, the sediment is treated as a non-
71 Newtonian flow while the seawater as a Newtonian flow, both solved according to either
72 Navier-Stokes equations [3, 4] or simplified governing equations such as the shallow water
73 theory [5, 6]. Despite of the prevalence of this solution strategy (particularly for modelling

74 submarine landslide generated tsunami), it fails to capture the solid-like features of subsea
75 sediments and thus does not perform well for the stability analysis of underwater slopes or for
76 the analysis of their progressive failure behaviour. Recent efforts made in this regard include
77 [7-9] in which simulations were carried out in the framework of solid (or soil) mechanics.
78 Owing to the low permeability, material clays in these works were represented by the Tresca
79 or Von-Mises constitutive model implying an undrained condition. The progressive
80 development of plastic shear deformation in marine clays was reproduced via the reduction of
81 undrained shear strength with accumulated plastic displacement or strain. Influence of
82 seawater on the submarine landslides in [7-9] was considered by using the submerged density
83 of the sediment. Such an approximation is only reasonable when the sliding proceeds in a
84 quasi-static process. Otherwise, the hydraulic effects from the seawater have to be taken into
85 account. A representative example rests with the phenomena in submarine landslides that a
86 layer of water intrudes under the sediment results in a lubrication effect and a decrease in the
87 resistance between the sediment and the seabed [10, 11]. This mechanism, termed as
88 hydroplaning, is deemed a reason for unexpectedly long travel distance of submarine
89 landslide, and its prediction obviously necessitates a fully coupled analysis of the seawater-
90 soil interaction. Apart from that, the rheological feature of the sediment was ignored in [7-9].
91 A remarkable contribution in this regard lies in [12] where the Storegga Slide was simulated
92 using a two-phase flow model. The interaction between the seawater and the sediment was
93 coupled in the framework of Computational Fluid Dynamics (CFD) that a Newtonian flow
94 model was applied for representing seawater and a non-Newtonian flow model for the
95 rheological behaviour of sediments. The solid behaviour of the sediment was somewhat
96 accounted for through deducing the threshold yield stress with plastic strains.
97
98 Indeed, the seawater-soil (or fluid-solid) coupled analysis is a challenge in the simulation of

99 submarine landslides. According to the solution scheme, the numerical approaches for a
100 fluid-solid interaction problem may be broadly categorised into the monolithic approach and
101 the partitioned approach. The monolithic approach attempts to remould the entire problem
102 (e.g. fluids and solids) into a single system equation that can be resolved via a unified
103 algorithm [13, 14]. The fluid and the solid in such a manner thus are coupled implicitly with
104 the interfacial conditions being fulfilled naturally within the solution procedure. Although
105 better accuracy for multidisciplinary problems can be achieved via this coupling strategy,
106 unifying multidisciplinary problems is never a trivial task and requires more expertise. For
107 the submarine landslides concerned, the difficulty of unification will be further enhanced
108 since more sophisticated soil models are required aiming to capture the complex behaviour of
109 sediments. The partitioned approach [15, 16], on the other hand, solves the fluid dynamics
110 and the solid mechanics separately. Communications in between is achieved through explicit
111 enforcement of interfacial conditions to each solution with convergence being expected via
112 iteration loops. An apparent advantage of the partitioned approach is its capability of
113 handling multidisciplinary problems of complicated physics; nevertheless, tracking the
114 varying interface dividing the fluid and solid domains, which is not known a priori, is
115 burdensome.

116

117 In this paper, we provide a computational framework that is capable of modelling submarine
118 landslides and their consequences. The framework unifies the finite element formulations for
119 both the fluid (seawater) and the solid (sediments and offshore infrastructure) dynamics and
120 thus their coupling can be achieved naturally in a monolithic manner. Utilisation of complex
121 constitutive soil models is also possible in this framework. The final monolithically coupled
122 formulation is then merged into the Particle Finite Element Method to tackle issues resulting
123 from extreme deformation such as mesh distortion and free-surface evolution. The proposed

124 approach is verified against numerous benchmarks and its possibility for modelling the entire
 125 process of a submarine landslide from failure triggering through transportation to deposition
 126 in a single seamless simulation is demonstrated. Its capability in the evaluation of the direct
 127 impact of a submarine landslide on offshore infrastructure such as gas pipelines and the
 128 indirect impact via generating a tsunami is also shown.

129

130 The paper is organized as follows. Section 2 presents the standard formulation for the second-
 131 order cone programming (SOCP) problem that the finite element formulation for solids/fluids
 132 will be remoulded into. The procedures for the reformulation of the discretised governing
 133 equations for fluids and solids into an optimisation problem are then presented in Sections 3
 134 and 4, respectively. Section 5 details the scheme for coupling the solid and the fluid using the
 135 mixed finite element and and Section 6 briefly introduces the particle finite element method.
 136 Numerical examples are given in Section 7 for demonstrating the correctness and robustness
 137 of the proposed approach before conclusions are drawn in Section 8.

138

139 2. Second-order Cone Programming

140

141 Second-order cone programming (SOCP), also referred as conic quadratic optimisation, is a
 142 generalisation of linear and quadratic programming that allows the variables to be constrained
 143 inside second-order cones. When there are no linear inequality constraints, a standard SOCP
 144 program involves an optimisation problem of the form

145

$$\begin{aligned}
 & \min_{\mathbf{x}} \quad \mathbf{c}^T \mathbf{x} \\
 & \text{subject to} \quad \mathbf{Ax} = \mathbf{b} \\
 & \quad \quad \quad \mathbf{x} \hat{\in} K
 \end{aligned} \tag{1}$$

147 where $\mathbf{x} = (x_1, x_2, \dots, x_m)^T$ is the vector consisting of the field variables and K is a tensorial

148 product of second-order cones such that $K = K_1' K_2' \dots K_s$. The cones may be in a type of

- 149 • the quadratic:

150
$$K_q = \left\{ x \in \mathbb{R}^m \mid x_1^2 \leq \sqrt{x_2^2 + L + x_m^2} \right\} \quad (2)$$

151 or

- 152 • the rotated quadratic:

153
$$K_r = \left\{ x \in \mathbb{R}^m \mid 2x_1x_2 \leq x_3^2 + L + x_m^2, x_1, x_2 \geq 0 \right\} \quad (3)$$

154

155 Numerous problems have so far been remoulded as a SOCP problem. Typical examples
156 include computational limit analysis of solids and plates [17-19], static/dynamic analysis of
157 elastoplastic/elastoviscoplastic frames and solids [20-22], deformation and consolidation
158 analysis of porous media [23], particle dynamic simulations (e.g. discrete element method or
159 granular contact dynamics) [24-26], and fracture in brittle rocks [27] and jointed rock [28]
160 among others. This implies that problems in different fields may be resolved efficiently using
161 a single solver, which is particularly favourable when parallel computing is in need.
162 Comparing to the contributions in solid regime, less efforts have been devoted to the
163 reformulation of fluid dynamics problems except in [29] where steady yield flows were
164 analysis in SOCP.

165

166

167 3. Mathematical programming formulation of Newtonian/Non-Newtonian fluids

168

169 This section aims to reformulate the governing equations of Newtonian or Non-Newtonian
 170 fluids, after time distretisation, into a standard optimisation problem. Unlike in [29] that a
 171 steady flow was considered, the dynamic non-steady Newtonian/Non-Newtonian flows are
 172 concerned. Additionally, a generalised Hellinger-Reissner variational principle rather than the
 173 minimum principle is adopted in this paper so that the optimisation problem raised for fluid
 174 dynamics possess the same design variables as those for solid dynamics for the sake of
 175 convenience for their monolithic coupling.

176

177 3.1 Governing equations

178 We herein first consider the Bingham flow which is a typical non-Newtonian model. In case
 179 of incompressibility, the governing equations for a Bingham flow (with Einstein's notations)
 180 are as follows according to [29]:

$$181 \quad \sigma_{ij,j} + b_i = \rho \ddot{u}_i \quad (4)$$

$$182 \quad \dot{u}_{i,i} = 0 \quad (5)$$

$$183 \quad \dot{\epsilon}_{ij} = \frac{1}{2}(\dot{u}_{i,j} + \dot{u}_{j,i}) \quad (6)$$

$$184 \quad \begin{cases} \dot{\epsilon}_{ij} = 0 & \text{if } \sqrt{\frac{1}{2}s_{ij}s_{ij}} < \tau_0 \\ s_{ij} = 2\mu \dot{\epsilon}_{ij} + \tau_0 \frac{\dot{\epsilon}_{ij}}{|\dot{\epsilon}_{ij}|} & \text{if } \sqrt{\frac{1}{2}s_{ij}s_{ij}} \geq \tau_0 \end{cases} \quad \text{in } \Omega \quad (7)$$

185 where σ_{ij} is the stress tensor, $\dot{\epsilon}_{ij}$ is the strain rate tensor, b_i is the volume body force, ρ is
186 the density of the fluid, u_i is the displacement with a superposed dot representing
187 differentiation with respect to time, $s_{ij} = dev(\sigma_{ij}) = \sigma_{ij} - \frac{1}{3}\sigma_{kk}\delta_{ij}$ is the deviatoric stress
188 tensor. Equations in (7) is the constitutive model for a Bingham flow distinguishing a rigid
189 region from a yield one where μ is a constant viscosity efficiency, τ_0 is the threshold stress
190 for yielding and $|\dot{\epsilon}_{ij}| = \sqrt{\frac{1}{2}\dot{\epsilon}_{ij}\dot{\epsilon}_{ij}}$. It is obvious that the above governing equations degrade to
191 those for a standard Newtonian flow when $\tau_0 = 0$.

192

193 In order to recast the formulation using the Hellinger-Reissner variational principle, the
194 constitutive equations are rewritten as a more general form (similar to those in solid
195 mechanics)

$$196 \quad \sigma_{ij} = \tau_{ij} + 2\mu\dot{\epsilon}_{ij} \quad (8)$$

$$197 \quad \dot{\epsilon}_{ij} = \dot{\lambda} \frac{\partial F(\tau_{ij})}{\partial \tau_{ij}} \quad (9)$$

$$198 \quad \dot{\lambda} F(\tau_{ij}) = 0; \dot{\lambda} \geq 0; F(\tau_{ij}) \leq 0 \quad (10)$$

199 where $\dot{\lambda}$ is the rate of the non-negative plastic multiplier, F in this case is the Von Mises
200 yield function (e.g. $F(\sigma_{ij}) = \sqrt{\frac{1}{2}s_{ij}s_{ij}} - \tau_0$), τ_{ij} is the stress lying on the boundary of F (e.g.
201 $F(\tau_{ij}) = 0$) and the quantity $\sigma_{ij} - \tau_{ij}$ is called the overstress which is null when $F(\sigma_{ij}) \leq 0$.

202

203 To prove the equivalence between the set of constraints (8)-(10) and the constitutive model in
204 (7), condition (9) is first expressed as

$$205 \quad \dot{\epsilon}_{ij} = \dot{\lambda} \frac{dev(\tau_{ij})}{2\tau_0} \quad (11)$$

206 via the substitution of the following relations

207
$$F(\tau_{ij}) = \sqrt{\frac{1}{2} dev(\tau_{ij}) dev(\tau_{ij})} - \tau_0 = 0 \quad (12)$$

208
$$\frac{\partial F(\tau_{ij})}{\partial \tau_{ij}} = \frac{dev(\tau_{ij})}{\sqrt{2 dev(\tau_{ij}) dev(\tau_{ij})}} \quad (13)$$

209 For the von Mises criterion, the incompressible condition $\dot{\epsilon}_{kk} = 0$ always holds and
 210 meanwhile Eq. (8) may be rewritten as

211
$$2\mu \dot{\epsilon}_{ij} = s_{ij} - dev(\tau_{ij}) \quad (14)$$

212 The deviatoric part of τ_{ij} is proportional to the rate of shear strain tensor $\dot{\epsilon}_{ij}$, namely

213
$$\frac{dev(\tau_{ij})}{|dev(\tau_{ij})|} = \frac{\dot{\epsilon}_{ij}}{|\dot{\epsilon}_{ij}|} \quad (15)$$

214 Because τ_{ij} is located on the yield surface that $F(\tau_{ij}) = 0$, we have $|dev(\tau_{ij})| = \tau_0$. Thus, Eq.
 215 (15) can then be expressed as

216
$$dev(\tau_{ij}) = \tau_0 \frac{\dot{\epsilon}_{ij}}{|\dot{\epsilon}_{ij}|} \quad \text{if } F(\sigma_{ij}) > 0 \quad (16)$$

217 Substituting Eq. (16) into Eq. (14) renders

218
$$2\mu \dot{\epsilon}_{ij} = s_{ij} - \tau_0 \frac{\dot{\epsilon}_{ij}}{|\dot{\epsilon}_{ij}|} \quad \text{if } F(\sigma_{ij}) > 0 \quad (17)$$

219 which is the second constraint in (7). When $F(\sigma_{ij}) < 0$ is fulfilled (which also means
 220 $F(\tau_{ij}) < 0$ since $\sigma_{ij} = \tau_{ij}$ in this case), constraints in (10) indicate a null plastic strain, that is
 221 also the total strain in this case, which is in line with the first constraint in (7). Thus the set of
 222 equations (8)-(10) is equivalent to the constitutive model in (7). Using vector-matrix
 223 notations, the governing equations for a Bingham flow can now be expressed in a more
 224 general form of

225
$$\nabla^T \boldsymbol{\sigma} + \mathbf{b} = \rho \ddot{\mathbf{u}} \quad (18)$$

226
$$\dot{\boldsymbol{\epsilon}} = \nabla^T \dot{\mathbf{u}} \quad (19)$$

227
$$\boldsymbol{\sigma} = \boldsymbol{\tau} + 2\mu\dot{\boldsymbol{\epsilon}} \quad (20)$$

228
$$\dot{\boldsymbol{\epsilon}} = \dot{\lambda} \frac{\partial F(\boldsymbol{\tau})}{\partial \boldsymbol{\tau}}; \dot{\lambda} F(\boldsymbol{\tau}) = 0; \dot{\lambda} \geq 0; F(\boldsymbol{\tau}) \leq 0 \quad (21)$$

229 supplemented by boundary conditions

230
$$\mathbf{u} = \bar{\mathbf{u}} \quad \text{on } \Gamma_u \quad (22)$$

231
$$\mathbf{N}^T \boldsymbol{\sigma} = \bar{\mathbf{t}} \quad \text{on } \Gamma_t \quad (23)$$

232 where $\bar{\mathbf{u}}$ and $\bar{\mathbf{t}}$ are the prescribed displacements and external tractions, \mathbf{N} consists of
 233 components of the outward normal to the boundary Γ_t and ∇^T is the transposed gradient
 234 operator. Notably, the incompressible condition in Eq. (5) does not need to be included
 235 explicitly since the utilisation of Von Mises model implies null volumetric change.

236

237 3.2 Time discretisation

238 Since a direct-time integration approach will be used for dynamic analysis, the governing
 239 equations (18)-(23) have to be discretised before the equivalent variational principle is
 240 proposed. Using the standard θ -method, the momentum conservation equation (18) and the
 241 natural boundary condition (23) is discretized in time as:

242
$$\nabla^T [\theta_1 \boldsymbol{\sigma}_{n+1} + (1 - \theta_1) \boldsymbol{\sigma}_n] + \mathbf{b} = \rho \frac{\mathbf{v}_{n+1} - \mathbf{v}_n}{\Delta t} \quad (24)$$

243
$$\theta_2 \mathbf{v}_{n+1} + (1 - \theta_2) \mathbf{v}_n = \frac{\mathbf{u}_{n+1} - \mathbf{u}_n}{\Delta t} \quad (25)$$

244
$$\mathbf{N}^T (\theta_1 \boldsymbol{\sigma}_{n+1} + (1 - \theta_1) \boldsymbol{\sigma}_n) = \bar{\mathbf{t}}_{n+1} \quad \text{on } \Gamma_t \quad (26)$$

245 where \mathbf{v} are velocities, θ_1 and θ_2 are parameters taking values in $[0, 1]$, the subscripts n and
 246 $n+1$ refer to the known and new, unknown states, and $\Delta t = t_{n+1} - t_n$ is the time step.
 247 Rearranging the above equations leads to

248
$$\nabla^T \boldsymbol{\sigma}_{n+1} + \frac{1-\theta_1}{\theta_1} \nabla^T \boldsymbol{\sigma}_n + \tilde{\mathbf{b}} = \tilde{\rho} \frac{\Delta \mathbf{u}}{\Delta t^2} \quad (27)$$

249
$$\mathbf{v}_{n+1} = \frac{1}{\theta_2} \left[\frac{\Delta \mathbf{u}}{\Delta t} - (1-\theta_2) \mathbf{v}_n \right] \quad (28)$$

250
$$\mathbf{N}^T (\boldsymbol{\sigma}_{n+1} + \frac{1-\theta_1}{\theta_1} \boldsymbol{\sigma}_n) = \tilde{\mathbf{t}} \quad \text{on } \Gamma_t \quad \text{with } \tilde{\mathbf{t}} = \frac{1}{\theta_1} \bar{\mathbf{t}}_{n+1} \quad (29)$$

251 where $\Delta \mathbf{u} = \mathbf{u}_{n+1} - \mathbf{u}_n$ are the displacement increments and

252
$$\tilde{\mathbf{b}} = \frac{1}{\theta_1} \mathbf{b} + \tilde{\rho} \frac{\mathbf{v}_n}{\Delta t} \quad \text{with } \tilde{\rho} = \frac{\rho}{\theta_1 \theta_2} \quad (30)$$

253 The essential boundary condition is

254
$$\mathbf{u}_{n+1} = \bar{\mathbf{u}}_{n+1} \quad \text{on } \Gamma_u \quad (31)$$

255 The constitutive equations of the Bingham model can also be discretised by introducing a
256 parameter $\theta_3 \in [0, 1]$:

257
$$(\boldsymbol{\sigma}_n + \theta_3 \Delta \boldsymbol{\sigma}) - (\boldsymbol{\tau}_n + \theta_3 \Delta \boldsymbol{\tau}) = \mu \frac{\Delta \boldsymbol{\varepsilon}}{\Delta t} \Rightarrow (\Delta \boldsymbol{\sigma} - \Delta \boldsymbol{\tau}) + \frac{1}{\theta_3} (\boldsymbol{\sigma}_n - \boldsymbol{\tau}_n) = \frac{\mu}{\theta_3 \Delta t} \Delta \boldsymbol{\varepsilon} \quad (32)$$

258
$$\Delta \boldsymbol{\varepsilon} = \nabla^T (\Delta \mathbf{u}) = \Delta \lambda \nabla_{\boldsymbol{\tau}} F(\boldsymbol{\tau}_{n+1}) \quad (33)$$

259
$$F(\boldsymbol{\tau}_{n+1}) \leq 0; \Delta \lambda \geq 0; \Delta \lambda F(\boldsymbol{\tau}_{n+1}) = 0 \quad (34)$$

260 In summary, the governing equations for incremental analysis of Bingham flows consist of
261 conditions in (27), (29), and (31)-(34). The velocity at the end of each incremental analysis
262 can be updated according to Eq. (28) explicitly. The Newtonian flow is recovered by setting
263 the threshold stress $\tau_0 = 0$.

264

265 3.3 Generalised Hellinger-Reissner variational principle

266

267 A generalized Hellinger-Reissner (HR) variational principle is established in this section for
 268 the increment analysis of the reformulated Bingham flow problem. In HR principle, both
 269 displacements and stresses are master fields, which is in contrast to the principle of minimum
 270 potential energy in which displacements are the only master field. More specifically, the
 271 generalised HR variational principle is in the form of a min-max program:

$$\begin{aligned}
 & \min_{\Delta \mathbf{u}} \max_{(\boldsymbol{\sigma}, \boldsymbol{\tau}, \mathbf{r})_{n+1}} \int_{\Omega} \boldsymbol{\sigma}_{n+1}^T \nabla^T (\Delta \mathbf{u}) d\Omega + \int_{\Omega} \frac{1-\theta_1}{\theta_1} \boldsymbol{\sigma}_n^T \nabla^T (\Delta \mathbf{u}) d\Omega \\
 & - \frac{1}{2} \int_{\Omega} \mathbf{r}_{n+1}^T \frac{\Delta t^2}{\tilde{\rho}} \mathbf{r}_{n+1} d\Omega + \int_{\Omega} \mathbf{r}_{n+1}^T \Delta \mathbf{u} d\Omega \\
 & - \frac{1}{2} \int_{\Omega} (\Delta \boldsymbol{\sigma} - \Delta \boldsymbol{\tau})^T \frac{\theta_3 \Delta t}{\mu} (\Delta \boldsymbol{\sigma} - \Delta \boldsymbol{\tau}) d\Omega - \int_{\Omega} \Delta \boldsymbol{\sigma}^T \frac{\Delta t}{\mu} (\boldsymbol{\sigma}_n - \boldsymbol{\tau}_n) d\Omega \\
 & + \int_{\Omega} (\boldsymbol{\sigma}_n - \boldsymbol{\tau}_n)^T \frac{\Delta t}{\mu} \Delta \boldsymbol{\tau} d\Omega - \int_{\Omega} \tilde{\mathbf{b}}^T \Delta \mathbf{u} d\Omega - \int_{\Gamma_t} \tilde{\mathbf{t}}^T \Delta \mathbf{u} d\Gamma \\
 & \text{subject to } F(\boldsymbol{\tau}_{n+1}) \leq 0
 \end{aligned} \tag{35}$$

273 where $\Delta \mathbf{u}$, $\boldsymbol{\sigma}$, $\boldsymbol{\tau}$, and \mathbf{r} (a set of new variables representing the dynamic force) are master
 274 fields. To prove the equivalence between the principle (36) and the relevant discretised
 275 governing equations, the inequality constraint in (37) is first transferred into an equality one as

$$\begin{aligned}
 & \min_{\Delta \mathbf{u}} \max_{(\boldsymbol{\sigma}, \boldsymbol{\tau}, \mathbf{r})_{n+1}} \int_{\Omega} \boldsymbol{\sigma}_{n+1}^T \nabla^T (\Delta \mathbf{u}) d\Omega + \int_{\Omega} \frac{1-\theta_1}{\theta_1} \boldsymbol{\sigma}_n^T \nabla^T (\Delta \mathbf{u}) d\Omega \\
 & - \frac{1}{2} \int_{\Omega} \mathbf{r}_{n+1}^T \frac{\Delta t^2}{\tilde{\rho}} \mathbf{r}_{n+1} d\Omega + \int_{\Omega} \mathbf{r}_{n+1}^T \Delta \mathbf{u} d\Omega \\
 & - \frac{1}{2} \int_{\Omega} (\Delta \boldsymbol{\sigma} - \Delta \boldsymbol{\tau})^T \frac{\theta_3 \Delta t}{\mu} (\Delta \boldsymbol{\sigma} - \Delta \boldsymbol{\tau}) d\Omega - \int_{\Omega} \Delta \boldsymbol{\sigma}^T \frac{\Delta t}{\mu} (\boldsymbol{\sigma}_n - \boldsymbol{\tau}_n) d\Omega \\
 & + \int_{\Omega} (\boldsymbol{\sigma}_n - \boldsymbol{\tau}_n)^T \frac{\Delta t}{\mu} \Delta \boldsymbol{\tau} d\Omega - \int_{\Omega} \tilde{\mathbf{b}}^T \Delta \mathbf{u} d\Omega - \int_{\Gamma_t} \tilde{\mathbf{t}}^T \Delta \mathbf{u} d\Gamma + \int_{\Omega} \beta \ln s_{n+1} d\Omega \\
 & \text{subject to } F(\boldsymbol{\tau}_{n+1}) + s_{n+1} = 0
 \end{aligned} \tag{38}$$

277 by introducing a positively-restricted variable s_{n+1} where β is an arbitrarily small positive
 278 constant. This transformation is typical when resolving an optimisation problem in
 279 mathematical programming.

280

281 The Lagrangian associated with the optimisation problem (38) is

$$\begin{aligned}
& L_f(\Delta \mathbf{u}, \boldsymbol{\sigma}_{n+1}, \boldsymbol{\tau}_{n+1}, \mathbf{r}_{n+1}, \Delta \lambda, s_{n+1}) \\
& = \int_{\Omega} \boldsymbol{\sigma}_{n+1}^T \nabla^T(\Delta \mathbf{u}) d\Omega + \int_{\Omega} \frac{1-\theta_1}{\theta_1} \boldsymbol{\sigma}_n^T \nabla^T(\Delta \mathbf{u}) d\Omega - \frac{1}{2} \int_{\Omega} \mathbf{r}_{n+1}^T \frac{\Delta t^2}{\tilde{\rho}} \mathbf{r}_{n+1} d\Omega + \int_{\Omega} \mathbf{r}_{n+1}^T \Delta \mathbf{u} d\Omega \\
282 & - \frac{1}{2} \int_{\Omega} (\Delta \boldsymbol{\sigma} - \Delta \boldsymbol{\tau})^T \frac{\theta_3 \Delta t}{\mu} (\Delta \boldsymbol{\sigma} - \Delta \boldsymbol{\tau}) d\Omega - \int_{\Omega} \Delta \boldsymbol{\sigma}^T \frac{\Delta t}{\mu} (\boldsymbol{\sigma}_n - \boldsymbol{\tau}_n) d\Omega + \int_{\Omega} (\boldsymbol{\sigma}_n - \boldsymbol{\tau}_n)^T \frac{\Delta t}{\mu} \Delta \boldsymbol{\tau} d\Omega \\
& - \int_{\Omega} \tilde{\mathbf{b}}^T \Delta \mathbf{u} d\Omega - \int_{\Gamma_t} \tilde{\mathbf{t}}^T \Delta \mathbf{u} d\Gamma + \int_{\Omega} \beta \ln s_{n+1} d\Omega - \int_{\Omega} \Delta \lambda (F(\boldsymbol{\tau}_{n+1}) + s_{n+1}) d\Omega
\end{aligned} \tag{39}$$

283 whose variation with respect to the optimisation variables gives:

$$284 \quad \frac{\partial L_f}{\partial \Delta \mathbf{u}} = \begin{cases} \nabla^T \boldsymbol{\sigma}_{n+1} + \frac{1-\theta_1}{\theta_1} \nabla^T \boldsymbol{\sigma}_n + \mathbf{r}_{n+1} - \tilde{\mathbf{b}} = \mathbf{0} & \text{in } \Omega \\ \mathbf{N}^T (\boldsymbol{\sigma}_{n+1} + \frac{1-\theta_1}{\theta_1} \boldsymbol{\sigma}_n) = \tilde{\mathbf{t}} & \text{on } \Gamma_t \end{cases} \tag{40}$$

$$285 \quad \frac{\partial L_f}{\partial \boldsymbol{\sigma}_{n+1}} = \nabla^T(\Delta \mathbf{u}) - \frac{\theta_3 \Delta t}{\mu} (\Delta \boldsymbol{\sigma} - \Delta \boldsymbol{\tau}) - \frac{\Delta t}{\mu} (\boldsymbol{\sigma}_n - \boldsymbol{\tau}_n) = \mathbf{0} \quad \text{in } \Omega \tag{41}$$

$$286 \quad \frac{\partial L_f}{\partial \boldsymbol{\tau}_{n+1}} = \frac{\theta_3 \Delta t}{\mu} (\Delta \boldsymbol{\sigma} - \Delta \boldsymbol{\tau}) + \frac{\Delta t}{\mu} (\boldsymbol{\sigma}_n - \boldsymbol{\tau}_n) - \Delta \lambda \nabla_{\boldsymbol{\tau}} F(\boldsymbol{\tau}_{n+1}) = \mathbf{0} \quad \text{in } \Omega \tag{42}$$

$$287 \quad \frac{\partial L_f}{\partial \mathbf{r}_{n+1}} = \frac{\Delta t^2}{\tilde{\rho}} \mathbf{r}_{n+1} - \Delta \mathbf{u} = \mathbf{0} \quad \text{in } \Omega \tag{43}$$

$$288 \quad \frac{\partial L_f}{\partial \Delta \lambda} = F(\boldsymbol{\tau}_{n+1}) + s_{n+1} = 0 \quad \text{in } \Omega \tag{44}$$

$$289 \quad \frac{\partial L_f}{\partial s_{n+1}} = \beta s_{n+1}^{-1} - \Delta \lambda = 0 \Rightarrow \beta = s_{n+1} \Delta \lambda \quad \text{in } \Omega \tag{45}$$

290 Because of the non-negative nature of $\Delta \lambda$, the last two KKT conditions (e.g. (44) and (45))

291 associated with the optimisation problem recover the yield condition and the

292 complementarity condition shown in (34) when $\beta \rightarrow 0^+$. The rest of the KKT conditions (e.g.

293 Eqs. (40)-(43)) are apparently the discretised governing equations presented in section 3.2
 294 (e.g. Eqs. (27), (29), (32) and (33)). Thus, the min-max optimisation problem (35) is
 295 equivalent to the discretised governing equations for the Bingham flow or those for
 296 Newtonian flow when the threshold stress τ_0 in the yield criterion of (35) is null.

297

298 4. Mathematical programming formulation of solid dynamics

299

300 Since the governing equations for the non-Newtonian flow are expressed in a general form,
 301 the extension of the relevant optimisation problem to the one for an elastoviscoplastic solid is
 302 forthright. The governing equations for the dynamics of an elastoviscoplastic solid are the
 303 same as those for fluid dynamics expect for the differences in the constitutive equations. The
 304 constitutive equations for an elastoviscoplastic solid are

$$305 \quad \boldsymbol{\sigma} = \boldsymbol{\tau} + 2\mu\dot{\boldsymbol{\epsilon}}^{\text{vp}} \quad (46)$$

$$306 \quad \dot{\boldsymbol{\epsilon}} = \nabla^T \dot{\mathbf{u}} = \dot{\boldsymbol{\epsilon}}^e + \dot{\boldsymbol{\epsilon}}^{\text{vp}} \quad (47)$$

$$307 \quad \dot{\boldsymbol{\epsilon}}^e = \mathbf{f} \dot{\boldsymbol{\sigma}} \quad (48)$$

$$308 \quad \dot{\boldsymbol{\epsilon}}^{\text{vp}} = \dot{\lambda} \frac{\partial F(\boldsymbol{\tau})}{\partial \boldsymbol{\tau}}; \dot{\lambda} F(\boldsymbol{\tau}) = 0; \dot{\lambda} \geq 0 \quad (49)$$

309 which, along with the momentum balance equation (18) and the boundary conditions (22) and
 310 (23), compose the complete governing equations for the relevant dynamic analysis. Again,
 311 the constitutive equations are similar to those for Bingham flows except that, according to
 312 (47), the rate of the total strain rate $\dot{\boldsymbol{\epsilon}}$ is divided into an elastic part $\dot{\boldsymbol{\epsilon}}^e$, that is related to the
 313 stress via the Hooke's law (48) with \mathbf{f} being elastic compliance matrix, and a viscoplastic
 314 part $\dot{\boldsymbol{\epsilon}}^{\text{vp}}$ calculated using the rule of plastic flow (49). This is in contrast to the case in section
 315 3 that any strain induced refers to unrecoverable 'plastic strain'. Thus the min-max problem
 316 (35) only needs to further include the elastic part for incremental elastoviscoplastic analysis

317 of a solid which is

$$\begin{aligned}
\min_{\Delta \mathbf{u}} \max_{(\boldsymbol{\sigma}, \boldsymbol{\tau}, \mathbf{r})_{n+1}} & \quad \underbrace{-\frac{1}{2} \int_{\Omega} \Delta \boldsymbol{\sigma}^T \square \Delta \boldsymbol{\sigma} d\Omega}_{\text{Elasticity}} + \int_{\Omega} \boldsymbol{\sigma}_{n+1}^T \nabla^T (\Delta \mathbf{u}) d\Omega + \int_{\Omega} \frac{1-\theta_1}{\theta_1} \boldsymbol{\sigma}_n^T \nabla^T (\Delta \mathbf{u}) d\Omega \\
& \quad - \frac{1}{2} \int_{\Omega} \mathbf{r}_{n+1}^T \frac{\Delta t^2}{\tilde{\rho}} \mathbf{r}_{n+1} d\Omega + \int_{\Omega} \mathbf{r}_{n+1}^T \Delta \mathbf{u} d\Omega \\
& \quad - \frac{1}{2} \int_{\Omega} (\Delta \boldsymbol{\sigma} - \Delta \boldsymbol{\tau})^T \frac{\theta_3 \Delta t}{\mu} (\Delta \boldsymbol{\sigma} - \Delta \boldsymbol{\tau}) d\Omega - \int_{\Omega} \Delta \boldsymbol{\sigma}^T \frac{\Delta t}{\mu} (\boldsymbol{\sigma}_n - \boldsymbol{\tau}_n) d\Omega \\
& \quad + \int_{\Omega} (\boldsymbol{\sigma}_n - \boldsymbol{\tau}_n)^T \frac{\Delta t}{\mu} \Delta \boldsymbol{\tau} d\Omega - \int_{\Omega} \tilde{\mathbf{b}}^T \Delta \mathbf{u} d\Omega - \int_{\Gamma_t} \tilde{\mathbf{t}}^T \Delta \mathbf{u} d\Gamma
\end{aligned} \tag{50}$$

318

subject to $F(\boldsymbol{\tau}_{n+1}) \leq 0$

319 The associated Lagrangian, after the transition of the inequality constraint into an equality
320 one as carried out in the last section, is expressed as

$$L_s(\Delta \mathbf{u}, \boldsymbol{\sigma}_{n+1}, \boldsymbol{\tau}_{n+1}, \mathbf{r}_{n+1}, \Delta \lambda, s_{n+1}) = -\frac{1}{2} \int_{\Omega} \Delta \boldsymbol{\sigma}^T \square \Delta \boldsymbol{\sigma} d\Omega + L_f \tag{51}$$

321

322 whose variation with respect to $\boldsymbol{\sigma}_{n+1}$ and $\boldsymbol{\tau}_{n+1}$ gives

$$\frac{\partial L_s}{\partial \boldsymbol{\sigma}_{n+1}} = \nabla^T (\Delta \mathbf{u}) - \underbrace{\square \Delta \boldsymbol{\sigma}}_{\text{Elastic strain}} - \underbrace{\frac{\theta_3 \Delta t}{\mu} (\Delta \boldsymbol{\sigma} - \Delta \boldsymbol{\tau}) - \frac{\Delta t}{\mu} (\boldsymbol{\sigma}_n - \boldsymbol{\tau}_n)}_{\text{Viscoplastic strain}} = \mathbf{0} \quad \text{in } \Omega \tag{52}$$

323

$$\frac{\partial L_s}{\partial \boldsymbol{\tau}_{n+1}} = \frac{\partial L_f}{\partial \boldsymbol{\tau}_{n+1}} = \underbrace{\frac{\theta_3 \Delta t}{\mu} (\Delta \boldsymbol{\sigma} - \Delta \boldsymbol{\tau}) + \frac{\Delta t}{\mu} (\boldsymbol{\sigma}_n - \boldsymbol{\tau}_n)}_{\text{Viscoplastic strain}} - \Delta \lambda \nabla_{\boldsymbol{\tau}} F(\boldsymbol{\tau}_{n+1}) = \mathbf{0} \quad \text{in } \Omega \tag{53}$$

324

325 Substitution of Eq. (53) into (52) results in the addition decomposition of the total strain rate
326 for example Eq. (47). The variation of L_s with respect to other variables (e.g. $\Delta \mathbf{u}$, \mathbf{r}_{n+1} , $\Delta \lambda$,
327 and s_{n+1}) results in Eqs. (40), (43)-(45), which verifies the equivalence between the
328 optimisation problem (50) and the discretised governing equations for dynamic analysis of an
329 elastoviscoplastic solid.

330

331 Material hardening/softening behaviour can also be accounted for in the principle according

332 to [22]. Suppose that a yield criterion function with strain hardening/softening is in the form
 333 of $F(\boldsymbol{\tau}, \boldsymbol{\kappa}) = 0$ where $\boldsymbol{\kappa} = H(\boldsymbol{\epsilon}^{vp})$ is a set of internal variables relating to the viscoplastic
 334 strain. The associated principle according to [22] thus is

335

$$\begin{aligned}
 \min_{\Delta \mathbf{u}} \max_{(\boldsymbol{\sigma}, \boldsymbol{\tau}, \mathbf{r}, \boldsymbol{\kappa})_{n+1}} & -\frac{1}{2} \int_{\Omega} \Delta \boldsymbol{\sigma}^T \square \Delta \boldsymbol{\sigma} d\Omega + \int_{\Omega} \boldsymbol{\sigma}_{n+1}^T \nabla^T (\Delta \mathbf{u}) d\Omega + \int_{\Omega} \frac{1-\theta_1}{\theta_1} \boldsymbol{\sigma}_n^T \nabla^T (\Delta \mathbf{u}) d\Omega \\
 & -\frac{1}{2} \int_{\Omega} \mathbf{r}_{n+1}^T \frac{\Delta t^2}{\tilde{\rho}} \mathbf{r}_{n+1} d\Omega + \int_{\Omega} \mathbf{r}_{n+1}^T \Delta \mathbf{u} d\Omega \\
 336 & -\frac{1}{2} \int_{\Omega} (\Delta \boldsymbol{\sigma} - \Delta \boldsymbol{\tau})^T \frac{\theta_3 \Delta t}{\eta} (\Delta \boldsymbol{\sigma} - \Delta \boldsymbol{\tau}) d\Omega - \int_{\Omega} \Delta \boldsymbol{\sigma}^T \frac{\Delta t}{\eta} (\boldsymbol{\sigma}_n - \boldsymbol{\tau}_n) d\Omega \quad (54) \\
 & + \int_{\Omega} (\boldsymbol{\sigma}_n - \boldsymbol{\tau}_n)^T \frac{\Delta t}{\eta} \Delta \boldsymbol{\tau} d\Omega - \underbrace{\frac{1}{2} \int_{\Omega} H_t^{-1} \Delta \boldsymbol{\kappa}^2 d\Omega}_{\text{Hardening/Softening term}} - \int_{\Omega} \tilde{\mathbf{b}}^T \Delta \mathbf{u} d\Omega - \int_{\Gamma_t} \tilde{\mathbf{t}}^T \Delta \mathbf{u} d\Gamma \\
 \text{subject to} & \quad F(\boldsymbol{\tau}_{n+1}, \underline{\boldsymbol{\kappa}}_{n+1}) \leq 0
 \end{aligned}$$

337 where the underlined terms are newly introduced due to the hardening/softening and H_t is
 338 constitutive modulus that reads

$$339 \quad H_t = -\frac{dH(\boldsymbol{\epsilon}_n^{vp})}{d\boldsymbol{\epsilon}^{vp}} \frac{\nabla_{\boldsymbol{\tau}} F(\boldsymbol{\tau}_n, \boldsymbol{\kappa}_n)}{\nabla_{\boldsymbol{\kappa}} F(\boldsymbol{\tau}_n, \boldsymbol{\kappa}_n)} \quad (55)$$

340 The inclusion of material hardening/softening in the principle have been detailed in [22] and
 341 thus is not further discussed in this paper.

342

343 In brief, variational principle (54) thus is a general optimisation problem for
 344 elastoviscoplastic analysis which degrades to principle (35)

$$\begin{aligned}
& \min_{\Delta \mathbf{u}} \max_{(\boldsymbol{\sigma}, \boldsymbol{\tau}, \mathbf{r})_{n+1}} \int_{\Omega} \boldsymbol{\sigma}_{n+1}^T \nabla^T (\Delta \mathbf{u}) d\Omega + \int_{\Omega} \frac{1-\theta_1}{\theta_1} \boldsymbol{\sigma}_n^T \nabla^T (\Delta \mathbf{u}) d\Omega \\
& - \frac{1}{2} \int_{\Omega} \mathbf{r}_{n+1}^T \frac{\Delta t^2}{\tilde{\rho}} \mathbf{r}_{n+1} d\Omega + \int_{\Omega} \mathbf{r}_{n+1}^T \Delta \mathbf{u} d\Omega \\
& - \frac{1}{2} \int_{\Omega} (\Delta \boldsymbol{\sigma} - \Delta \boldsymbol{\tau})^T \frac{\theta_3 \Delta t}{\mu} (\Delta \boldsymbol{\sigma} - \Delta \boldsymbol{\tau}) d\Omega - \int_{\Omega} \Delta \boldsymbol{\sigma}^T \frac{\Delta t}{\mu} (\boldsymbol{\sigma}_n - \boldsymbol{\tau}_n) d\Omega \\
& + \int_{\Omega} (\boldsymbol{\sigma}_n - \boldsymbol{\tau}_n)^T \frac{\Delta t}{\mu} \Delta \boldsymbol{\tau} d\Omega - \int_{\Omega} \tilde{\mathbf{b}}^T \Delta \mathbf{u} d\Omega - \int_{\Gamma_t} \tilde{\mathbf{t}}^T \Delta \mathbf{u} d\Gamma \\
& \text{subject to } F(\boldsymbol{\tau}_{n+1}) \leq 0
\end{aligned}$$

345

346 for the incremental analysis of Newtonian/Non-Newtonian flows when the parts relevant to
347 the elasticity and material hardening/softening are erased. When the Von Mises yield
348 criterion is used, the above problem is for analysing the standard Bingham flow. While the
349 threshold stress is null, it recovers the Newtonian flow.

350

351 Moreover, principle (54) degrades to cover the rate-independent elastoplastic dynamic
352 analysis by erasing the terms related to viscosity that is

$$\begin{aligned}
& \min_{\Delta \mathbf{u}} \max_{(\boldsymbol{\sigma}, \mathbf{r}, \kappa)_{n+1}} -\frac{1}{2} \int_{\Omega} \Delta \boldsymbol{\sigma}^T \square \Delta \boldsymbol{\sigma} d\Omega + \int_{\Omega} \boldsymbol{\sigma}_{n+1}^T \nabla^T (\Delta \mathbf{u}) d\Omega + \int_{\Omega} \frac{1-\theta_1}{\theta_1} \boldsymbol{\sigma}_n^T \nabla^T (\Delta \mathbf{u}) d\Omega \\
& - \frac{1}{2} \int_{\Omega} \mathbf{r}_{n+1}^T \frac{\Delta t^2}{\tilde{\rho}} \mathbf{r}_{n+1} d\Omega + \int_{\Omega} \mathbf{r}_{n+1}^T \Delta \mathbf{u} d\Omega - \frac{1}{2} \int_{\Omega} \mathbf{H}_t^{-1} \Delta \kappa^2 d\Omega \\
& - \int_{\Omega} \tilde{\mathbf{b}}^T \Delta \mathbf{u} d\Omega - \int_{\Gamma_t} \tilde{\mathbf{t}}^T \Delta \mathbf{u} d\Gamma \\
& \text{subject to } F(\boldsymbol{\sigma}_{n+1}, \kappa_{n+1}) \leq 0
\end{aligned} \tag{56}$$

353

354 and to cover the elastoplastic static analysis [20] by further erasing the dynamic terms that is

$$\begin{aligned}
& \min_{\Delta \mathbf{u}} \max_{(\boldsymbol{\sigma}, \kappa)_{n+1}} -\frac{1}{2} \int_{\Omega} \Delta \boldsymbol{\sigma}^T \square \Delta \boldsymbol{\sigma} d\Omega + \int_{\Omega} \boldsymbol{\sigma}_{n+1}^T \nabla^T (\Delta \mathbf{u}) d\Omega - \frac{1}{2} \int_{\Omega} \mathbf{H}_t^{-1} \Delta \kappa^2 d\Omega \\
& - \int_{\Omega} \mathbf{b}^T \Delta \mathbf{u} d\Omega - \int_{\Gamma_t} \mathbf{t}_{n+1}^T \Delta \mathbf{u} d\Gamma \\
& \text{subject to } F(\boldsymbol{\sigma}_{n+1}, \kappa_{n+1}) \leq 0
\end{aligned} \tag{57}$$

355

356 The upper bound limit analysis [20, 30] is also recovered by deducting the elastic part and
357 hardening/softening part, which is

$$\begin{aligned}
358 \quad & \min_{\Delta \mathbf{u}} \max_{(\boldsymbol{\sigma}, \alpha)} \int_{\Omega} \boldsymbol{\sigma}^T \nabla^T (\Delta \mathbf{u}) d\Omega - \int_{\Omega} \mathbf{b}^T \Delta \mathbf{u} d\Omega - \alpha \int_{\Gamma_t} \mathbf{t}^T \Delta \mathbf{u} d\Gamma \\
& \text{subject to} \quad F(\boldsymbol{\sigma}) \leq 0
\end{aligned} \tag{58}$$

359 where α is a new introduced variable representing the factor of the imposed traction force.
360 Notably, all the above problems refer to total stress analysis. This is because the marine clay
361 is commonly simulated in undrained conditions [7, 9] according to its low permeability.
362 Nevertheless, the analysis of saturated porous media can also be casted into the same form
363 which has been discussed in [23] where the effective stress and pore water pressure instead of
364 the total stress should be the master fields.

365

366 5. Monolithic coupling and solution technique

367

368 The min-max problem (54) is first discretised using the standard finite element shape
369 function owing to its generalised feature, and then the coupling between the fluid and the
370 solid is discussed. As both the displacement-like and stress-like fields are master fields in the
371 generalised HR variational principle, they have to be interpolated by shape functions
372 independently such as

$$\begin{aligned}
373 \quad & \boldsymbol{\sigma}(\mathbf{x}) \approx \mathbf{N}_{\boldsymbol{\sigma}} \hat{\boldsymbol{\sigma}}, \quad \boldsymbol{\sigma}^e(\mathbf{x}) \approx \mathbf{N}_{\boldsymbol{\sigma}^e} \hat{\boldsymbol{\sigma}}^e, \quad \boldsymbol{\tau}(\mathbf{x}) \approx \mathbf{N}_{\boldsymbol{\tau}} \hat{\boldsymbol{\tau}}, \\
& \mathbf{r}(\mathbf{x}) \approx \mathbf{N}_{\mathbf{r}} \hat{\mathbf{r}}, \quad \mathbf{u}(\mathbf{x}) \approx \mathbf{N}_{\mathbf{u}} \hat{\mathbf{u}}, \quad \nabla^T \mathbf{u} \approx \mathbf{B}_{\mathbf{u}} \hat{\mathbf{u}}, \\
& \kappa(\mathbf{x}) \approx \mathbf{N}_{\kappa} \hat{\kappa}
\end{aligned} \tag{59}$$

374 where $\hat{\boldsymbol{\sigma}}$, $\hat{\boldsymbol{\sigma}}^e$, $\hat{\boldsymbol{\tau}}$, $\hat{\mathbf{r}}$, $\hat{\mathbf{u}}$, and $\hat{\kappa}$ are vectors containing the values of the corresponding field
375 variables at interpolation points, \mathbf{N} is a matrix consisting of shape functions, and $\mathbf{B}_{\mathbf{u}} = \nabla^T \mathbf{N}_{\mathbf{u}}$
376 .

377 By substituting Eq. (59), the principle (e.g. (54)) discretised in space reads

$$\begin{aligned}
\min_{\Delta \hat{\mathbf{u}}} \quad \max_{(\hat{\boldsymbol{\sigma}}, \hat{\boldsymbol{\tau}}, \hat{\boldsymbol{\sigma}}^e, \hat{\mathbf{r}}, \hat{\boldsymbol{\kappa}})_{n+1}} \quad & -\frac{1}{2} \Delta \hat{\boldsymbol{\sigma}}^T \mathbf{C} \Delta \hat{\boldsymbol{\sigma}} + \Delta \hat{\mathbf{u}}^T \mathbf{B}^T \hat{\boldsymbol{\sigma}}_{n+1} + \Delta \hat{\mathbf{u}}^T \frac{1-\theta_1}{\theta_1} \mathbf{B}^T \hat{\boldsymbol{\sigma}}_n \\
& -\frac{1}{2} \hat{\mathbf{r}}_{n+1}^T \mathbf{D} \hat{\mathbf{r}}_{n+1} + \Delta \hat{\mathbf{u}}^T \mathbf{A}^T \hat{\mathbf{r}}_{n+1} - \frac{1}{2} \Delta \hat{\boldsymbol{\sigma}}^{eT} \mathbf{M} \Delta \hat{\boldsymbol{\sigma}}^e \\
& -\Delta \hat{\boldsymbol{\sigma}}^{eT} \mathbf{f}^c - \frac{1}{2} \Delta \hat{\boldsymbol{\kappa}}^T \mathbf{H} \Delta \hat{\boldsymbol{\kappa}} - \Delta \hat{\mathbf{u}}^T \mathbf{f}^e
\end{aligned} \tag{60}$$

$$\text{subject to} \quad \Delta \hat{\boldsymbol{\sigma}}^e = \Delta \hat{\boldsymbol{\sigma}} - \Delta \hat{\boldsymbol{\tau}}$$

$$F_j(\hat{\boldsymbol{\tau}}_{n+1}, \hat{\boldsymbol{\kappa}}_{n+1}) \leq 0, \quad j=1, 2, \dots, N_G$$

where an intermediate variable $\boldsymbol{\sigma}^e = \boldsymbol{\sigma} - \boldsymbol{\tau}$ termed the overstress is introduced, N_G is the total number of integration points for instance Gauss points, and

$$\begin{aligned}
\mathbf{C} &= \int_{\Omega} \mathbf{N}_{\sigma}^T \mathbf{N}_{\sigma} d\Omega, \quad \mathbf{B}^T = \int_{\Omega} \mathbf{B}_u^T \mathbf{N}_{\sigma} d\Omega, \\
\mathbf{D} &= \int_{\Omega} \mathbf{N}_r^T \frac{\Delta t^2}{\tilde{\rho}} \mathbf{N}_r d\Omega, \quad \mathbf{A}^T = \int_{\Omega} \mathbf{N}_u^T \mathbf{N}_r d\Omega, \\
\mathbf{M} &= \int_{\Omega} \mathbf{N}_{\sigma^e}^T \frac{\theta_3 \Delta t}{\eta} \mathbf{N}_{\sigma^e} d\Omega, \quad \mathbf{H} = \int_{\Omega} \mathbf{N}_{\kappa}^T \frac{1}{H_t} \mathbf{N}_{\kappa} d\Omega, \\
\mathbf{f}^e &= \int_{\Omega} \mathbf{N}_u^T \tilde{\mathbf{b}} d\Omega + \int_{\Gamma_t} \mathbf{N}_u^T \tilde{\mathbf{t}} d\Gamma, \quad \mathbf{f}^c = \int_{\Omega} \mathbf{N}_{\sigma}^T \frac{\Delta t}{\eta} \boldsymbol{\sigma}_n^e d\Omega
\end{aligned} \tag{61}$$

The minimisation part of principle (60) with respect to the incremental displacement $\Delta \hat{\mathbf{u}}$ can be resolved analytically resulting in a maximisation problem which can also be expressed as a minimisation problem with an opposite sign

$$\begin{aligned}
\min_{(\hat{\boldsymbol{\sigma}}, \hat{\boldsymbol{\tau}}, \hat{\boldsymbol{\sigma}}^e, \hat{\mathbf{r}}, \hat{\boldsymbol{\kappa}})_{n+1}} \quad & \frac{1}{2} \Delta \hat{\boldsymbol{\sigma}}^T \mathbf{C} \Delta \hat{\boldsymbol{\sigma}} + \frac{1}{2} \hat{\mathbf{r}}_{n+1}^T \mathbf{D} \hat{\mathbf{r}}_{n+1} + \frac{1}{2} \Delta \hat{\boldsymbol{\sigma}}^{eT} \mathbf{M} \Delta \hat{\boldsymbol{\sigma}}^e \\
& + \frac{1}{2} \Delta \hat{\boldsymbol{\kappa}}^T \mathbf{H} \Delta \hat{\boldsymbol{\kappa}} + \Delta \hat{\boldsymbol{\sigma}}^{eT} \mathbf{f}^c \\
\text{subject to} \quad & \mathbf{B}^T \hat{\boldsymbol{\sigma}}_{n+1} + \frac{1-\theta_1}{\theta_1} \mathbf{B}^T \hat{\boldsymbol{\sigma}}_n + \mathbf{A}^T \hat{\mathbf{r}}_{n+1} - \mathbf{f}^e = \mathbf{0} \\
& \Delta \hat{\boldsymbol{\sigma}}^e = \Delta \hat{\boldsymbol{\sigma}} - \Delta \hat{\boldsymbol{\tau}} \\
& F_j(\hat{\boldsymbol{\tau}}_{n+1}, \hat{\boldsymbol{\kappa}}_{n+1}) \leq 0, \quad j=1, 2, \dots, N_G
\end{aligned} \tag{62}$$

The finite element discretised principle for Newtonian/Non-Newtonian flow can also be

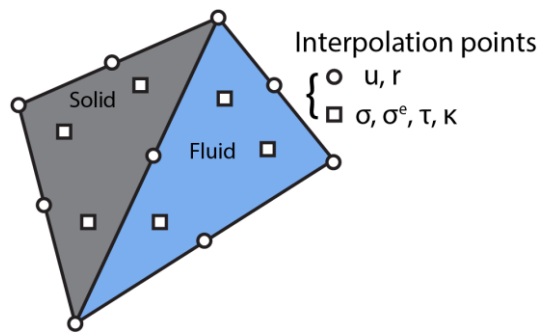
388 derived following the same way which is

$$\begin{aligned}
 & \min_{(\hat{\boldsymbol{\sigma}}, \hat{\boldsymbol{\tau}}, \hat{\boldsymbol{\sigma}}^e, \hat{\boldsymbol{r}})_{n+1}} \quad \frac{1}{2} \hat{\boldsymbol{r}}_{n+1}^T \mathbf{D} \hat{\boldsymbol{r}}_{n+1} + \frac{1}{2} \Delta \hat{\boldsymbol{\sigma}}^{eT} \mathbf{M} \Delta \hat{\boldsymbol{\sigma}}^e + \Delta \hat{\boldsymbol{\sigma}}^{eT} \mathbf{f}^c \\
 & \text{subject to} \quad \mathbf{B}^T \hat{\boldsymbol{\sigma}}_{n+1} + \frac{1-\theta_1}{\theta_1} \mathbf{B}^T \hat{\boldsymbol{\sigma}}_n + \mathbf{A}^T \hat{\boldsymbol{r}}_{n+1} - \mathbf{f}^c = \mathbf{0} \\
 & \quad \Delta \hat{\boldsymbol{\sigma}}^e = \Delta \hat{\boldsymbol{\sigma}} - \Delta \hat{\boldsymbol{\tau}} \\
 & \quad F_j(\hat{\boldsymbol{\tau}}_{n+1}) \leq 0, \quad j=1, 2, \dots, N_G
 \end{aligned} \tag{63}$$

390 The principles (62) and (63) can be solved for solids and fluids, respectively, or the
 391 coupling can be achieved by just solving the principle (62). In this study, the later strategy
 392 is adopted for the sake of convenience. More specifically, a mixed isoparametric triangular
 393 element shown in Figure 2 is used for the approximation for both the solid and the fluid.

394 The location of the internal interpolation points are $(\beta_{j-1}, \beta_j, \beta_{j+1}) = (\frac{1}{6}, \frac{4}{6}, \frac{1}{6})$, $j=1, 2, 3$, with
 395 β_j being the area coordinates. The master fields for both the solid and the fluid are the
 396 same; however, when the element represents a fluid, the elastic compliance matrix \mathbf{C} and
 397 the constitutive modulus matrix \mathbf{H} at the integration points in principle (62) is set to be null
 398 and consequently the discretised principle (63) for a fluid is recovered. By doing so, the
 399 coupling of the fluid and the solid is achieved naturally in a monolithic fashion.

400



401

402

Figure 2 The mixed triangular element used in the simulation

403

404

405 In this study, the discretised principle (62) is transferred into the standard SOCP problem,
 406 namely the optimisation problem (1). The principle (62) is in a general form of

$$\begin{aligned}
 & \min_{\mathbf{x}} \quad \mathbf{x}^T \mathbf{Q} \mathbf{x} + \mathbf{c}^T \mathbf{x} \\
 & \text{subject to} \quad \mathbf{A} \mathbf{x} = \mathbf{b} \\
 & \quad \quad \quad F(\mathbf{x}) \leq 0
 \end{aligned} \tag{64}$$

408 and the relevant transformation is straightforward. Introducing an auxiliary variable
 409 $w = \mathbf{x}^T \mathbf{Q} \mathbf{x}$ and intermediate variables $\xi = \mathbf{Q}^{\frac{1}{2}} \mathbf{x}$, problem (64) can be re-written as

$$\begin{aligned}
 & \min_{(\mathbf{x}, w, y, \xi)} \quad w + \mathbf{c}^T \mathbf{x} \\
 & \text{subject to} \quad 2wy^3 - \xi^T \xi \\
 & \quad \quad \quad \xi = \mathbf{Q}^{\frac{1}{2}} \mathbf{x}; \quad y = 1 \\
 & \quad \quad \quad \mathbf{A} \mathbf{x} = \mathbf{b} \\
 & \quad \quad \quad F(\mathbf{x}) \leq 0
 \end{aligned} \tag{65}$$

411 It is clear that optimisation problem (65) is of a linear objective function subject to linear
 412 equations, an inequality constraint (the first inequality) of a type of a rotated quadratic cone
 413 (3), and an inequality for yielding $F(\mathbf{x}) \leq 0$. To transfer problem (65) into a SOCP problem,
 414 the yield criterion function $F(\mathbf{x}) \leq 0$ has to be expressed as a cone. Numerous efforts have
 415 been devoted in this regard, and so far typical constitutive models such as the Mohr-
 416 Coulomb/Tresca model, the Drucker-Prager/von Mises model, the CamClay model etc.,
 417 have been reformulated successfully. We refer readers to [23, 31, 32] for more details. The
 418 resulting SOCP problem in this work is then resolved using the advanced interior-point
 419 method available at the high-performance optimisation engine MOSEK [33].

420

421 6. The particle finite element method (PFEM)

422

423 Since both seawater and subsea sediments undergo a large of geometry in submarine
 424 landslide, the above solution algorithm is implemented in the Particle Finite Element Method

425 (PFEM) [34] to tackle issues such as mesh distortions and free-surface evolution resulting
426 from large deformation. The PFEM makes use of the standard Lagrangian finite element
427 approach to solve the discretised governing equations on meshes. At the time point that
428 meshes have a certain degree of distortion, mesh topologies are erased leaving behind mesh
429 nodes treated as free particles. A new computational domain is then identified using the so-
430 called α -shape method [35] on the basis of the position of free particles followed by the
431 remeshing of the identified domain. State variables are then mapped from old meshes to new
432 meshes followed by a new incremental finite element analysis. More details about the utilised
433 PFEM strategy refers to [36]. To date, the PFEM has tackled numerous challenging problems
434 such as the modelling of multi-phase flows [37], fluid-structure interactions [38, 39], granular
435 flows [40-43], flow of fresh cement suspensions [44], penetration problems [43, 45, 46],
436 landslides [47, 48] and the generated waves [49], among others.

437

438 7. Numerical Examples

439 The correctness and robustness of the proposed unified solid/fluid finite element
440 formulation (62) is verified via simulating numerous benchmarks. First, single-phase
441 problems such as the water dam break, the annular viscometer problem, and the collapse of
442 aluminum bars are simulated in order to verify it for modelling Newtonian flows, Non-
443 Newtonian flows, and solid dynamics, respectively. Comparisons of our simulation results
444 against experimental data, analytical solutions, and also results using other numerical
445 approaches available in literatures are carried out. The efficiency of the proposed
446 monolithic coupling for simulating multi-phase problems is then tested against an
447 experimental test concerning the underwater granular collapse and the induced waves. Last
448 but not least, the possibility of the approach for modelling submarine landslides and their
449 consequences is shown by considering a model test in which the failure and the post-failure

450 processes of an underwater slope are predicted via a single simulation with both the direct
451 impact on infrastructure such as pipelines and the indirect impact via the generated-tsunami
452 being estimated. In all simulations, small enough mesh sizes and time steps are used to
453 obtain converged solutions.

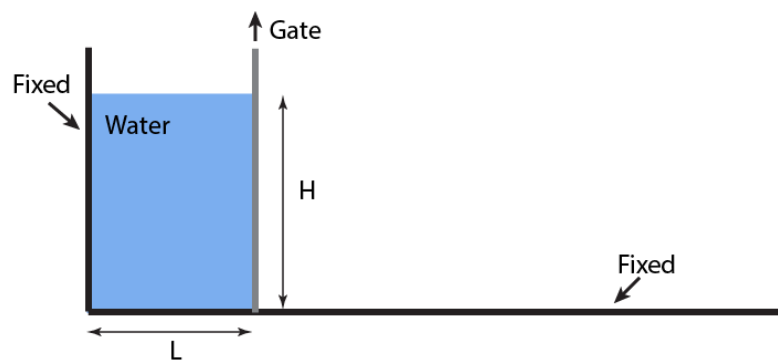
454

455 7.1 Single-phase problems

456 7.1.1 Newtonian flow

457 The first example concerned is the water dam break. The dam is initially 10 cm wide and 20
458 cm high as shown in Figure 3, and the water of density $\rho = 1 \times 10^3 \text{ kg/m}^3$ is incompressible.

459 The gravitational acceleration is $g = -9.8 \text{ m/s}^2$. The lift up of the gate leads to the spreading
460 of the water dam. As it is modelled as a Newtonian flow, the Von-Mises model is used with
461 the cohesion (or called threshold stress in the field of fluid dynamics) being null. The
462 domain is discretised using 3,879 triangular elements with typical element size $h = 0.4 \text{ cm}$
463 (e.g. the length of element edges). The parameters for time discretisation are $\theta_1 = \theta_2 = 1$, and
464 the time step utilised is $\Delta t = 1 \times 10^{-3} \text{ s}$.



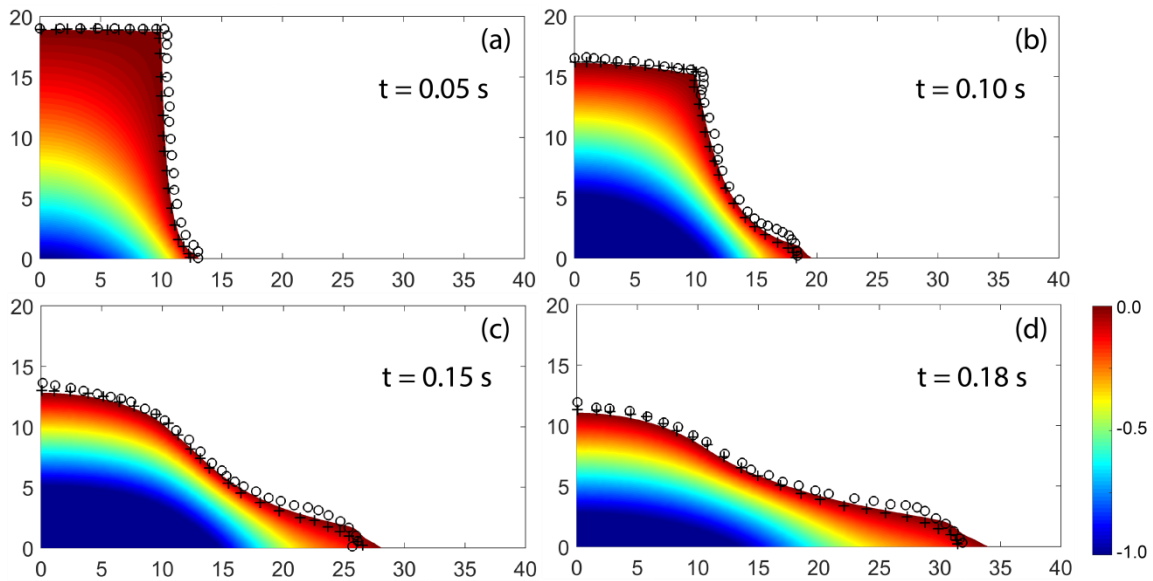
465

466 Figure 3 Schematic illustration of water dam break.

467

468 The configurations of the dam-break wave at four different time instants are plotted in
469 Figure 4 with the distribution of water pressure being shown. Simulation results from [50]
470 and [51], in which the Smooth Particle Hydrodynamics approach was used, are also

471 illustrated for comparison purposes in Figure 4. It is shown that the results agree with each
 472 other very well which verifies the proposed unified formulation for Newtonian flows.



473
 474 Figure 4 Configurations of the dam-break wave with the distribution of water pressure (unit:
 475 kPa) at time instances (a) $t = 0.05$ s, (b) $t = 0.10$ s; (c) $t = 0.15$ s, and (d) $t = 0.18$ s, respectively.
 476 Circles (o) represent the free surface obtained in [50], and crosses (+) refer to that obtained in
 477 [51].

478
 479 It is notable that the simulation does not suffer the issue of volumetric locking because of
 480 the used mixed elements that the displacement field is interpolated using quadratic shape
 481 functions and the stress field is approximated linearly.

482
 483 7.1.2 Non-Newtonian flow

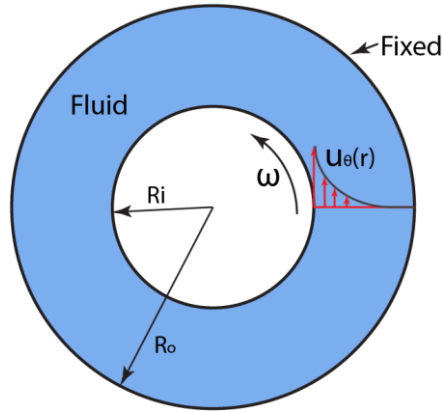
484 The Bingham flow in an annular viscometer is concerned for verifying the validity of the
 485 unified formulation for modelling Non-Newtonian flows in this section. The annular
 486 viscometer is made of two coaxial cylinders as shown in Figure 5. The out cylinder is fixed
 487 whereas the inner cylinder rotates in a constant angular velocity ω . Supposing the fluid is
 488 stick to the apparatus boundaries, analytical solutions are available which depend on the
 489 rheological properties of the fluid. For the considered Bingham fluid, a transition radius R_t
 490 exists that distinguishes the sheared fluids that are close to the inner cylinder from those

491 located in an un-yield/rigid zone. According to [52], the transition radius R_t is the solution
 492 of

$$493 \left(\frac{R_t}{R_i} \right)^2 - 2 \ln \left(\frac{R_t}{R_i} \right) - \left(\frac{2\sqrt{2}\mu\omega}{\tau_0} + 1 \right) = 0$$

494 and, in the sheared zone, the tangential velocity of the fluid is

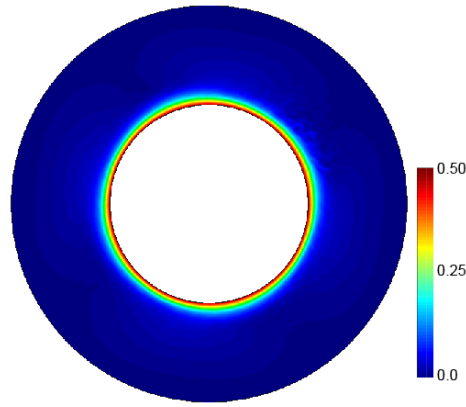
$$495 u_\theta(r) = r \frac{\sqrt{2}\tau_0}{\mu} \left(\left(\frac{R_t}{r} \right)^2 - 2 \ln \left(\frac{R_t}{r} \right) - 1 \right).$$



496
 497 Figure 5 A schematic illustration of an annular viscometer.

498 In this work, the radii of the outer and inner cylinders are $R_o = 100$ cm and $R_i = 50$ cm,
 499 respectively. The viscosity fluid is $\mu = 1$ Pa·s and the threshold stress $\tau_0 = 10$ Pa . The
 500 density is $\rho = 1000$ kg/m³. The inner cylinder rotates at an angular speed of $\omega = 1$ rad/s . The
 501 domain is discretised using meshes with a characteristic size $h = 3.5$ cm, and the time step
 502 for the simulation is $\Delta t = 1 \times 10^{-3}$ s.

504

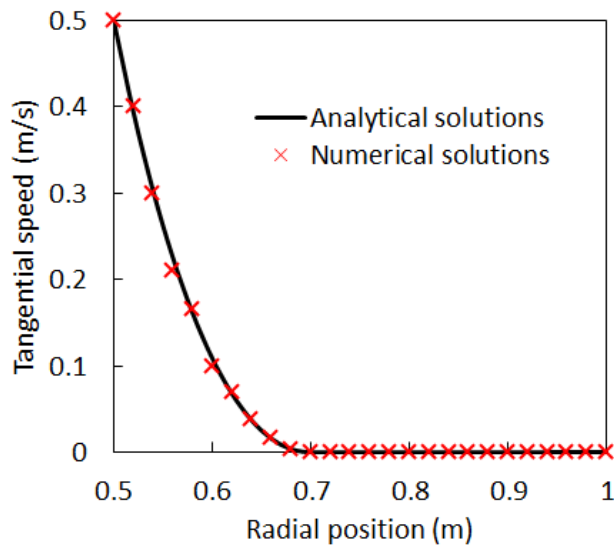


505

506

507 Figure 6 Distribution of the tangential speed at the steady state (Unit: m/s).

508



509

510 Figure 7 Curves of the tangential speed against the radial position.

511

512 Figure 6 shows the distribution of the speed at the steady state from our simulations. As
 513 expected, the tangential speed decreases with the radial position. Note that, although this a
 514 fluid dynamics problem in a fixed domain, issues related to sever mesh distortion still exist
 515 because the Lagrangian description/mesh is used. The corresponding tangential speed at the
 516 steady state is plotted in Figure 7. It is shown that the transition radius obtained from the
 517 simulation is around 0.7 m which coincides to the analytical solution. Furthermore, the
 518 overall tangential speed at the steady state from the simulation agrees well with the

519 analytical solution, indicating the correctness of the proposed unified formulation for Non-
520 Newtonian flows.

521

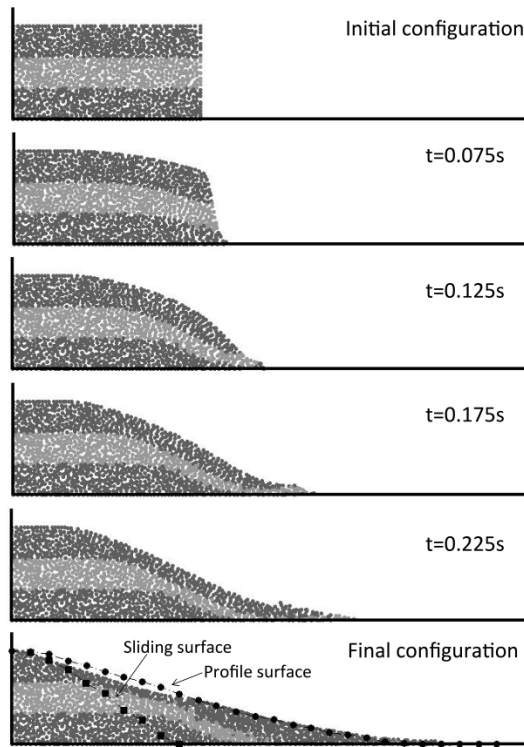
522 7.1.3 Solid mechanics problem

523 The third example for the single-phase problem is an experiment test of a collapse problem
524 conducted in [53] which is similar to the water break problem. The column of the size
525 200×100 mm however was composed of small aluminium bars of diameters 1 and 1.5 mm
526 and length 50 mm. This example was used to verify the SPH approach for simulating
527 elastoplastic problems in plane strain conditions in geomechanics in [53].

528

529 In our simulations, the Mohr-Coulomb model is used to represent the material with
530 parameters being the same as those from [53]: Young's Modulus $E = 0.84$ MPa , Poisson's
531 ratio $\nu = 0.3$, friction angle $\phi = 19.8^\circ$, dilation angle $\psi = 0^\circ$ and cohesion $c = 0$. The density
532 of the material is $\rho = 1.8 \times 10^3$ kg/m³ . The viscosity of the material is neglected in this case.

533 Simulations are carried out using a time step $\Delta t = 1 \times 10^{-3}$ s .



534

535 Figure 8 Snapshots of profiles at different time instances. The sliding surface and the profile
 536 surface are experimental data from [53].

537

538 Snapshots of configurations of the column at different time instances from our simulations
 539 are shown in Figure 8. The particles shown in the figure are mesh nodes marked in different
 540 colours. The lifting of the gate leads to an immediate collapse of the column. The top
 541 surface of the column is being eroded continuously throughout the collapse process whereas
 542 an undisturbed zone exists at the bottom left. The final profile as well as the surface of the
 543 undisturbed zone from our simulations are compared the experimental data [53]. As seen, a
 544 great agreement is achieved verifying the proposed unified model for solid dynamics.

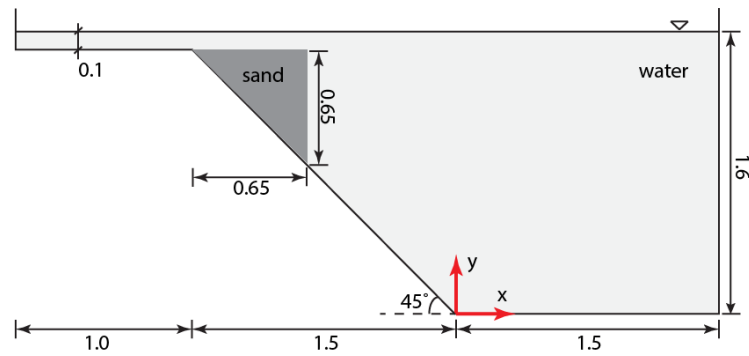
545

546 7.2 Multi-phase problem

547 The fourth example considered is a model test of submarine landslides and their hydraulic
 548 effects carried out by Rzadkiewicz et al. [54]. The setup is illustrated in Figure 9. As shown,
 549 the model test consists of a triangular mass of sands ($0.65 \text{ m} \times 0.65 \text{ m}$) that slide along an
 550 inclined surface of 45° in a water channel. The sand mass is initially positioned 0.1 m

551 below the water surface and its width is the same as that of the channel. The problem
 552 thus can be regarded plane-strain. This problem is commonly used for the validity of
 553 numerical approaches for multi-phase flows. In this study, it is used to verify the
 554 monolithic coupling of the proposed unified formulation for simulating multi-phase problem,
 555 in particular in terms of the water wave generated by submarine landslides.

556



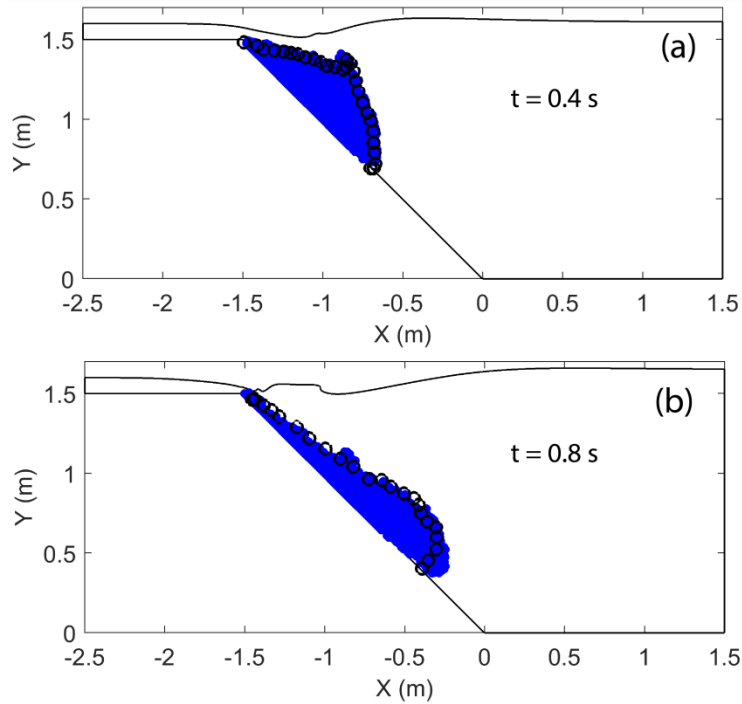
557

558 Figure 9 A schematic illustration of the experimental test for underwater granular flows
 559 (Unite of length: m).

560

561 In our simulation, the sand mass is approximated as a non-Newtonian fluid (e.g. Bingham
 562 flow) according to [54]. The material parameters used in our simulations are also in line
 563 with those in [54]. The density of water is 1000 kg/m^3 . Its viscosity and yield stress of water
 564 are null. The mean density of saturated sands is 1985 kg/m^3 and the threshold stress is 200
 565 Pa. The viscosity is null according to [54]. The characteristic mesh size used is $h = 0.015 \text{ m}$
 566 and the time step is $\Delta t = 1 \times 10^{-3} \text{ s}$.

567



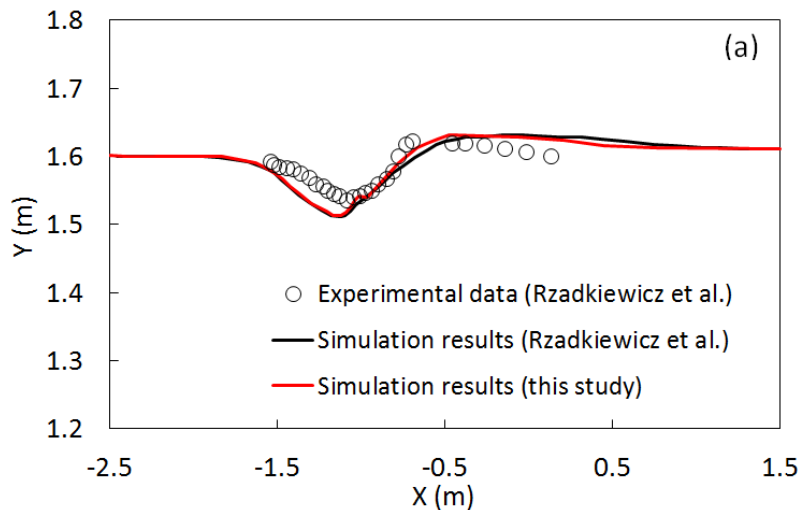
568

569 Figure 10 Snapshots of configurations of the sand mass and the induced water wave at time
 570 instance (a) $t = 0.4$ s and (b) $t = 0.8$ s. Circles are computed results from [54].

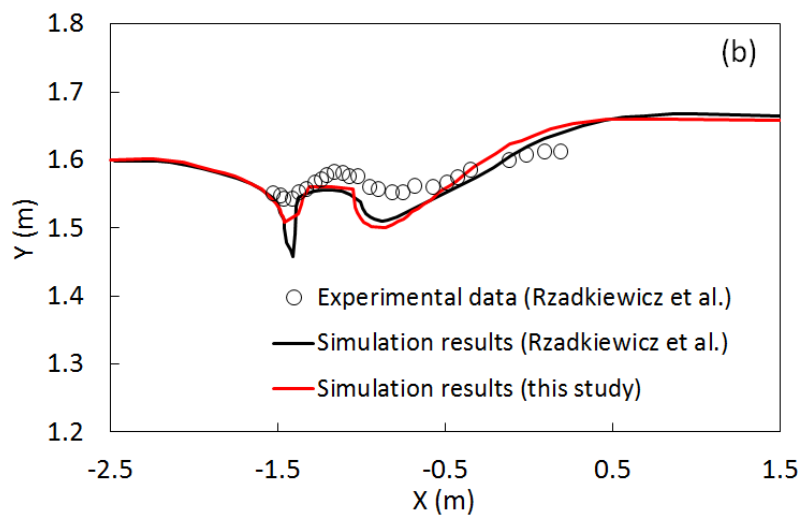
571

572 Figure 10 shows the snapshots of configurations of the sliding sand as well as the induced
 573 water wave at time instances of $t = 0.4$ s and 0.8 s, in which the corresponding shapes of
 574 deformed sand mass from the simulations in [54] are also shown for comparison. As shown,
 575 our simulated results agree well with those computed results from [54]. Moreover, Figure
 576 11 shows the quantitative comparison between the elevations of the free surface among our
 577 present simulation results, the computed results and the experimental data provided in [54]
 578 at those two time instances. Again, our simulations results coincide with the computed
 579 results from [54], both of which are close to the experimental data [54]. Such agreements
 580 verify the monolithic coupling of the proposed unified formulation for multi-phase
 581 problems.

582



583



584

585 Figure 11 Comparison of the elevations of the free surface at times (a) $t = 0.4$ s and (b) $t =$
 586 0.8 s.

587

588

589

7.3 Submarine landslides

590 Last but not least, the possibility of the proposed unified formulation for modelling

591 submarine landslides is presented via analysing an underwater slope failure and its

592 consequence. As shown in Figure 12, a marine clay slope of height 5 m and length 5 m is 3 m

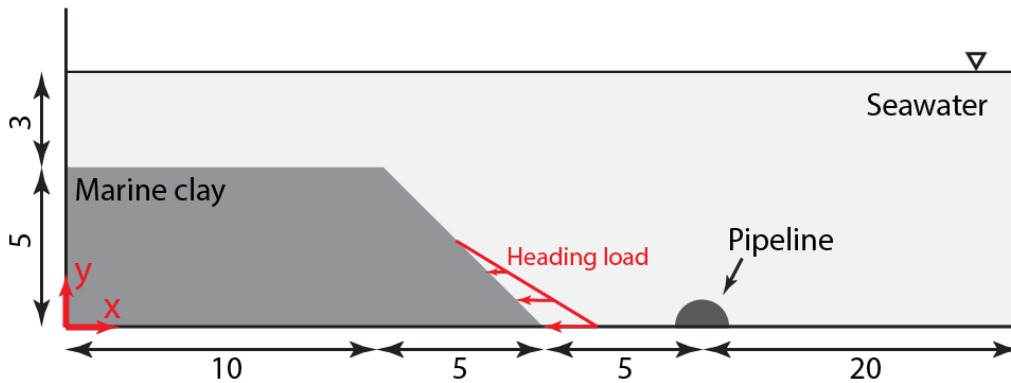
593 under the water surface. A half-buried pipeline of diameter 1.6 m is located 5 m in front of

594 the slope toe. Suppose the permeability of marine clays is very low so that the slope can be

595 simulated under undrained conditions The marine clays are represented by the Tresca model

596 with viscosity. The corresponding material parameters for the clay are as follows: Young's

597 modulus $E=3\times 10^7$ Pa, Poisson's ratio $\nu=0.49$, density $\rho_c=1.75\times 10^3$ kg/m³, undrained
 598 shear strength $c_u=6$ kPa and viscosity coefficient $\eta=50$ Pa·s. The density of seawater is
 599 $\rho_w=1\times 10^3$ kg/m³ and the viscosity coefficient is $\eta=0.001$ Pa·s. The gravitational
 600 acceleration is $g=-9.8$ m/s². The surfaces of the seabed and the pipeline are assumed to be
 601 rough.

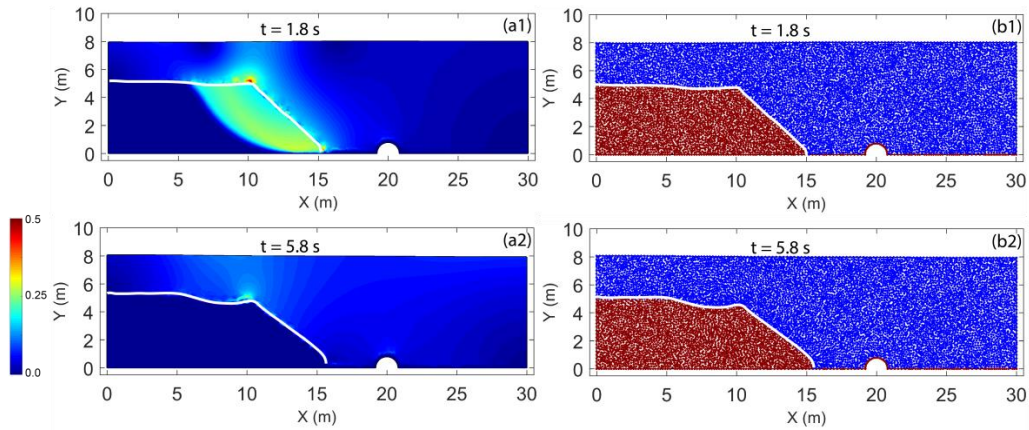


602

603 Figure 12 Schematic illustration of an underwater slope near a subsea pipeline (Unit of length:
 604 meter).

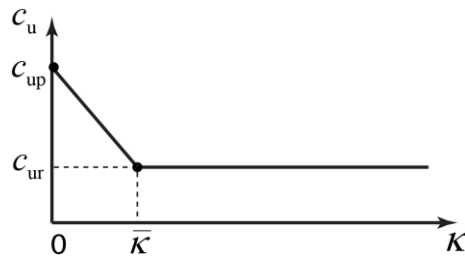
605

606 The slope was stable owing to the heading load which is then removed representing toe
 607 erosion. The factor of safety of the resulting slope is 0.90 implying instability. The problem
 608 is simulated using the proposed approach. The characteristic mesh size is 0.02 m leading to a
 609 total of 19,452 meshes (39,303 mesh nodes) for discretising the domains of marine clays and
 610 seawater. The time step used in the simulation is $\Delta t=5\times 10^{-3}$ s, and the simulation proceeds
 611 until the final deposit is obtained. As shown in Figure 13, the failure of the slope is triggered
 612 due to the removing of the heading load. The mass in the front slides along a failure surface
 613 but at a relatively low speed in this case (Figure 13(a1)). After a very limited deformation, the
 614 slope turns to be stable at a new position (Figure 13(a2)). Figure 13(b1) and (b2) indicate the
 615 corresponding layers of seawater and marine clays for comparison. Throughout the process,
 616 no obvious tsunami is generated.



617

618 Figure 13 Snapshots of the collapse process of the submarine landslide at different time
 619 instances from simulations without strain softening. Colors on the left figures are
 620 proportional to velocity (m/s) and figures on the right show the layers of the materials with
 621 blue and red colors representing seawater and marine clays, respectively. (Unit of speed: m/s)
 622



623

624 Figure 14 Variation of the undrained shear strength c_u with equivalent deviatoric plastic
 625 strain represented by parameter κ .

626

627

628 Notably, marine clay is normally sensitive which means its undrained strengths decreases
 629 from a peak value c_{up} to a residual one c_{ur} when the clay undergoes plastic deformation (see

630 Figure 14). It is reported in [8] that the sensitivity of marine clays, defined as $S_t = \frac{c_{up}}{c_{ur}}$, is

631 normally moderate. Herein the problem is re-analysed with the strain-softening feature being
 632 taken into account. The peak undrained strength is $c_{up} = 6$ kPa and the residual one is

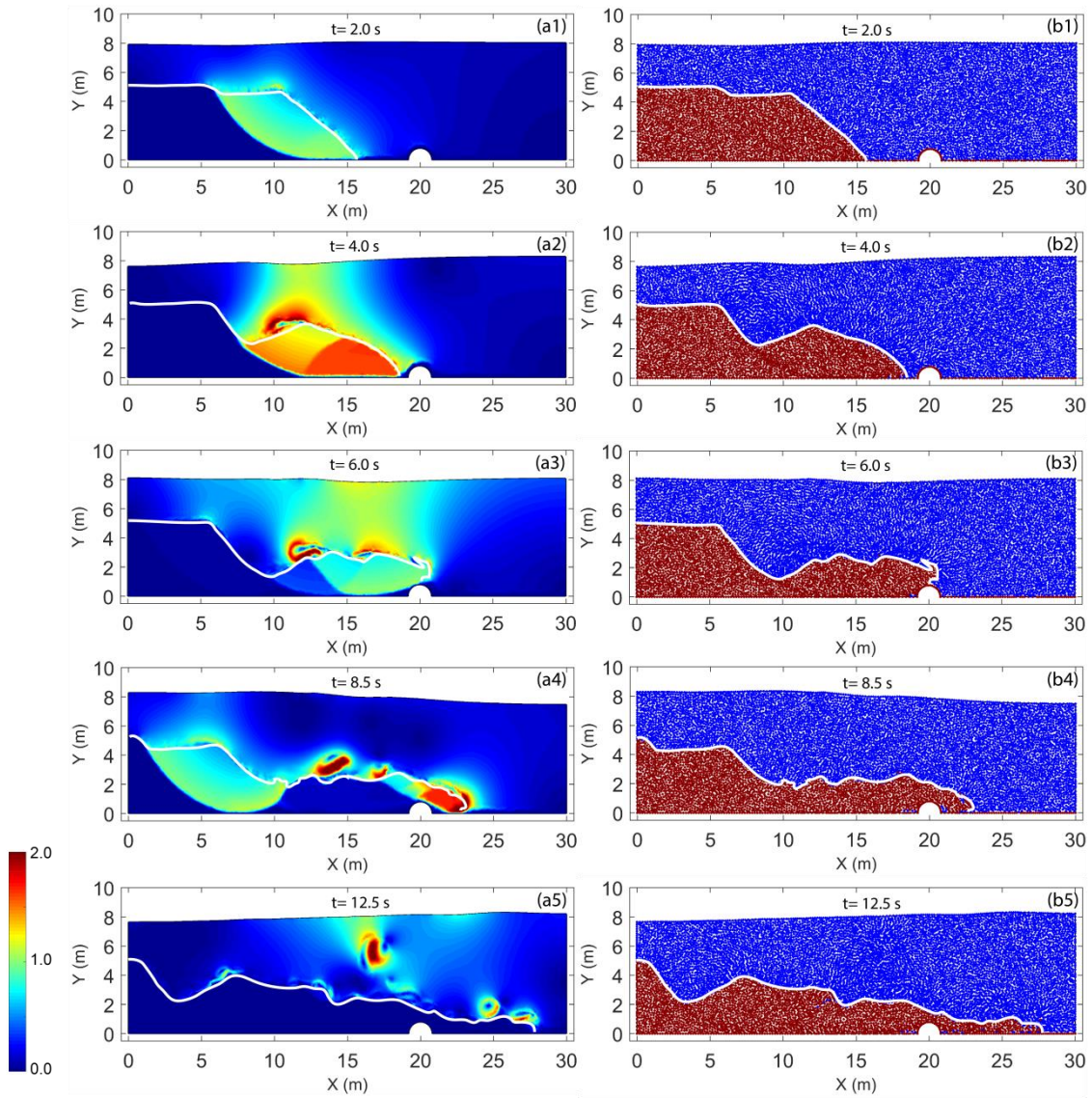
633 $c_{ur} = 1.5$ kPa, implying a moderate sensitivity ($S_t = 4$). The reference equivalent deviatoric
 634 plastic strain $\bar{\kappa}$, which controls the rate of the decrease of the undrained strain is set to be 0.6.

635 The complete process of the submarine landslides from the simulation is illustrated in Figure

636 15. The distribution of the sliding speed is shown in Figure 15(a) in which the white curves

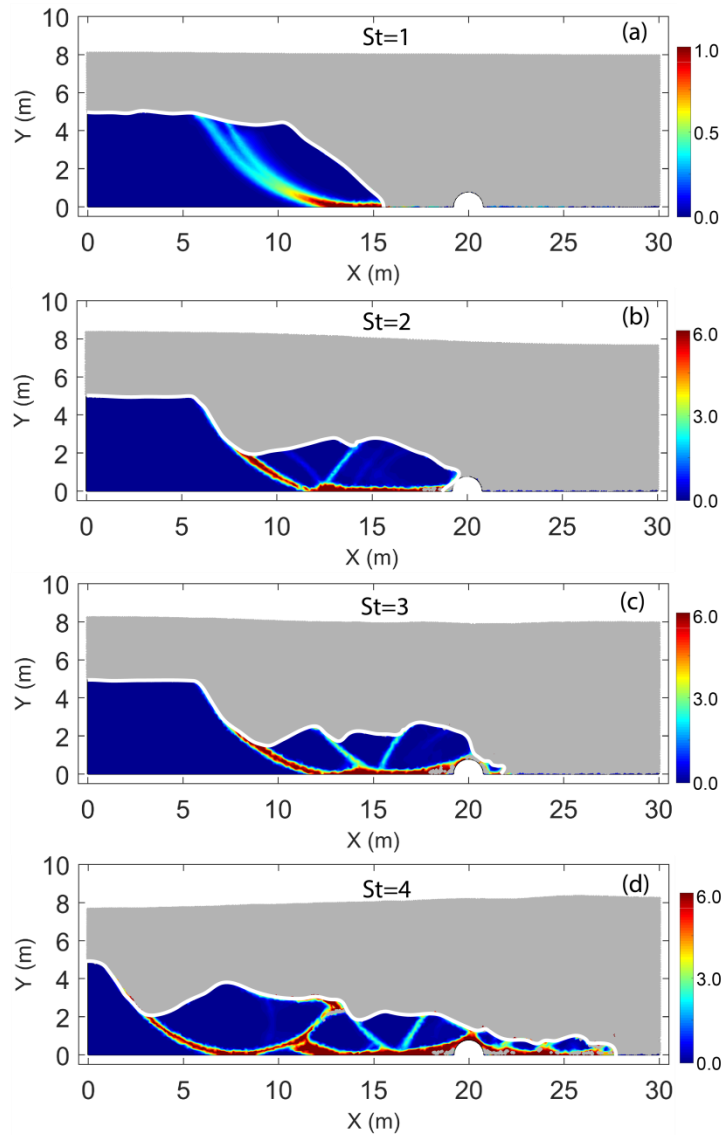
637 are the interface between the seawater and the clay drawn according to Figure 15(b) where
638 particles (mesh nodes) representing different materials are plotted. The same to the previous
639 case, the removing of the heading load triggers the failure of the slope as shown in Figure
640 15(a1) in which a shear band is expected along the failure surface. The clay evoked slides
641 along the failure surface and towards the pipeline (Figure 15(a2) and (b2)). At $t = 6.0\text{s}$, the
642 pipeline is impacted by the sliding mass (Figure 15(a3) and (b3)). When the evoked mass is
643 far enough from the newly generated back scarp of the slope, a second failure occurs as
644 shown in (Figure 15(a4) and (b4)). This feature is very typical for slope failure in sensitive
645 clays and is usually termed retrogressively progressive failure [55]. Eventually, the landslide
646 reaches its final deposition as shown in Figure 15(a5) and (b5). The failure of the underwater
647 slope in this case generates a clear tsunami in the process (Figure 15).

648
649 The effect of sensitivity of marine clays on the failure of a submarine slope is also
650 investigated by using different St . Figure 16 shows the final deposition of the landslides from
651 the simulation with St equal to 1, 2, 3, and 4, respectively. As shown, the slope is more prone
652 to fail when the sensitivity is large. Additionally, the sliding mass involved in each
653 retrogressive collapse is much easier to be further decomposed when sensitivity is higher.



654

655 Figure 15 Snapshots of the collapse process of the submarine landslide at different time
 656 instances from simulations with strain softening ($St=4$). Colors on the left figures are
 657 proportional to velocity (m/s) and figures on the right show the layers of the materials with
 658 blue and red colors representing seawater and marine clays, respectively. (Unit of speed: m/s)



659

660 Figure 16 Snapshots of final depositions of the submarine landslide from simulations with
 661 sensitivity of marine clays (a) $St=1$, (b) $St=2$, (c) $St=3$, and (d) $St=4$. Colors are proportional
 662 to equivalent deviatoric plastic strain.

663

664

665 8. Conclusions

666

667 This paper recasts the finite element formulation for fluid dynamics and solid mechanics into
 668 a unified elastoviscoplastic formulation. This is achieved by employing the generalised
 669 Hellinger-Reissner variational principle. The governing equations for both the fluid dynamics

670 and the solid mechanics are reformulated into a standard optimisation problem, namely a
671 min-max program, which then can be transformed into a second-order cone programming
672 problem and solved via advanced modern optimisation algorithm. In such a way, the coupling
673 between the solid and the fluid can be completed in a monolithic fashion which is particularly
674 importance for modelling submarine landslides. The resulting formulation is implemented in
675 the framework of the particle finite element method so that extreme deformation problems
676 can be simulated without any mesh distortion issue. A number of benchmarks of both single-
677 phase problems, involving Newtonian/Non-newtonian flows or solids, and multi-phase
678 problems, such as the model test on submarine landslide generated tsunamis, are simulated
679 using the proposed approach. Comparisons between the simulation results with available data
680 and analytical solutions are conducted where great agreements have been attained which
681 verifies the proposed method. Last but not least, a model test is considered to illustrate the
682 possibility of the proposed approach for modelling the consequences of submarine landslides
683 including their direct threat to offshore infrastructure such as pipelines and their indirect
684 threat via generating tsunamis. Sensitivity of the marine clays is also considered in this
685 example with its effect on the failure of underwater slope being shown.

686

687 **Acknowledgements** The authors wish to acknowledge the support The authors wish to
688 acknowledge the support of European Commission H2020 Marie Skłodowska-Curie actions
689 individual fellowship (Reference 744281).

690

691

692

693

- 695 1. Tappin, D.R., Watts, P., McMurtry, G.M., Lafoy, Y., and Matsumoto, T., The Sissano, Papua
696 New Guinea tsunami of July 1998 — offshore evidence on the source mechanism. *Marine*
697 *Geology*, 2001. **175**(1): p. 1-23.
- 698 2. Carter, L., Gavey, R., Talling, P.J., and Liu, J.T., Insights into Submarine Geohazards from
699 Breaks in Subsea Telecommunication Cables. *Oceanography* 2014. **27**(2): p. 58-67.
- 700 3. Capone, T., Panizzo, A., and Monaghan, J.J., SPH modelling of water waves generated by
701 submarine landslides. *Journal of Hydraulic Research*, 2010. **48**(sup1): p. 80-84.
- 702 4. Rzedkiewicz, S., Mariotti, C., and Heinrich, P., Numerical Simulation of Submarine Landslides
703 and Their Hydraulic Effects. *Journal of Waterway, Port, Coastal, and Ocean Engineering*,
704 1997. **123**(4): p. 149-157.
- 705 5. Heinrich, P.H., Piatanesi, A., and Hébert, H., Numerical modelling of tsunami generation and
706 propagation from submarine slumps: the 1998 Papua New Guinea event. *Geophysical*
707 *Journal International*, 2001. **145**(1): p. 97-111.
- 708 6. Didenkulova, I., Nikolkina, I., Pelinovsky, E., and Zahibo, N., Tsunami waves generated by
709 submarine landslides of variable volume: analytical solutions for a basin of variable depth.
710 *Nat. Hazards Earth Syst. Sci.*, 2010. **10**(11): p. 2407-2419.
- 711 7. Wang, D., Randolph, M.F., and White, D.J., A dynamic large deformation finite element
712 method based on mesh regeneration. *Computers and Geotechnics*, 2013. **54**: p. 192-201.
- 713 8. Dey, R., Hawlader, B., Phillips, R., and Soga, K., Modeling of large-deformation behaviour of
714 marine sensitive clays and its application to submarine slope stability analysis. *Canadian*
715 *Geotechnical Journal*, 2016. **53**(7): p. 1138-1155.
- 716 9. Dey, R., Hawlader, B.C., Phillips, R., and Soga, K., Numerical modelling of submarine
717 landslides with sensitive clay layers. *Géotechnique*, 2016. **66**(6): p. 454-468.
- 718 10. McAdoo, B.G., Pratson, L.F., and Orange, D.L., Submarine landslide geomorphology, US
719 continental slope. *Marine Geology*, 2000. **169**(1): p. 103-136.
- 720 11. Blasio, F.V.D., Engvik, L., Harbitz, C.B., and Elverhøi, A., Hydroplaning and submarine debris
721 flows. *Journal of Geophysical Research: Oceans*, 2004. **109**(C1).
- 722 12. Gauer, P., Kvalstad, T.J., Forsberg, C.F., Bryn, P., and Berg, K., The last phase of the Storegga
723 Slide: simulation of retrogressive slide dynamics and comparison with slide-scar morphology.
724 *Marine and Petroleum Geology*, 2005. **22**(1): p. 171-178.
- 725 13. Franci, A., Oñate, E., and Carbonell, J.M., Unified Lagrangian formulation for solid and fluid
726 mechanics and FSI problems. *Computer Methods in Applied Mechanics and Engineering*,
727 2016. **298**: p. 520-547.
- 728 14. Langer, U. and Yang, H., Robust and efficient monolithic fluid-structure-interaction solvers.
729 *International Journal for Numerical Methods in Engineering*, 2016. **108**(4): p. 303-325.
- 730 15. Degroote, J., Partitioned Simulation of Fluid-Structure Interaction. *Archives of Computational*
731 *Methods in Engineering*, 2013. **20**(3): p. 185-238.
- 732 16. R., R. and E., O., Analysis of some partitioned algorithms for fluid - structure interaction.
733 *Engineering Computations*, 2010. **27**(1): p. 20-56.
- 734 17. Le, C.V., Nguyen-Xuan, H., and Nguyen-Dang, H., Upper and lower bound limit analysis of
735 plates using FEM and second-order cone programming. *Computers & Structures*, 2010. **88**(1-
736 2): p. 65-73.
- 737 18. Makrodipopoulos, A. and Martin, C.M., Upper bound limit analysis using simplex strain
738 elements and second-order cone programming. *International Journal for Numerical and*
739 *Analytical Methods in Geomechanics*, 2007. **31**(6): p. 835-865.
- 740 19. Yu, S., Zhang, X., and Sloan, S.W., A 3D upper bound limit analysis using radial point
741 interpolation meshless method and second-order cone programming. *International Journal*
742 *for Numerical Methods in Engineering*, 2016. **108**(13): p. 1686-1704.
- 743 20. Krabbenhøft, K., Lyamin, A., and Sloan, S., Formulation and solution of some plasticity

- 744 problems as conic programs. *International Journal of Solids and Structures*, 2007. **44**(5): p.
745 1533-1549.
- 746 21. Yonekura, K. and Kanno, Y., Second-order cone programming with warm start for
747 elastoplastic analysis with von Mises yield criterion. *Optimization and Engineering*, 2012.
748 **13**(2): p. 181-218.
- 749 22. Zhang, X., Sheng, D., Sloan, S.W., and Bleyer, J., Lagrangian modelling of large deformation
750 induced by progressive failure of sensitive clays with elastoviscoplasticity. *International*
751 *Journal for Numerical Methods in Engineering*, 2017. **112**(8): p. 963-989.
- 752 23. Zhang, X., Sheng, D., Sloan, S.W., and Krabbenhoft, K., Second-order cone programming
753 formulation for consolidation analysis of saturated porous media. *Computational Mechanics*,
754 2016. **58**(1): p. 29-43.
- 755 24. Lim, K.-W., Krabbenhoft, K., and Andrade, J.E., A contact dynamics approach to the Granular
756 Element Method. *Computer Methods in Applied Mechanics and Engineering*, 2014. **268**: p.
757 557-573.
- 758 25. Krabbenhoft, K., Lyamin, A.V., and Vignes, C., Computational plasticity algorithm for particle
759 dynamics simulations. *Computational Particle Mechanics*, 2018. **5**(1): p. 103-111.
- 760 26. Krabbenhoft, K., Huang, J., da Silva, M.V., and Lyamin, A.V., Granular contact dynamics with
761 particle elasticity. *Granular Matter*, 2012. **14**(5): p. 607-619.
- 762 27. Meng, J., Huang, J., Yao, C., and Sheng, D., A discrete numerical method for brittle rocks
763 using mathematical programming. *Acta Geotechnica*, 2017.
- 764 28. Meng, J., Huang, J., Sloan, S.W., and Sheng, D., Discrete modelling jointed rock slopes using
765 mathematical programming methods. *Computers and Geotechnics*, 2018. **96**: p. 189-202.
- 766 29. Bleyer, J., Maillard, M., de Buhan, P., and Coussot, P., Efficient numerical computations of
767 yield stress fluid flows using second-order cone programming. *Computer Methods in Applied*
768 *Mechanics and Engineering*, 2015. **283**(0): p. 599-614.
- 769 30. Makrodimitopoulos, A. and Martin, C.M., Upper bound limit analysis using simplex strain
770 elements and second - order cone programming. *International Journal for Numerical and*
771 *Analytical Methods in Geomechanics*, 2007. **31**(6): p. 835-865.
- 772 31. Krabbenhoft, K. and Lyamin, A.V., Computational Cam clay plasticity using second-order
773 cone programming. *Computer Methods in Applied Mechanics and Engineering*, 2012. **209–**
774 **212**(0): p. 239-249.
- 775 32. Makrodimitopoulos, A., Remarks on some properties of conic yield restrictions in limit analysis.
776 *International Journal for Numerical Methods in Biomedical Engineering*, 2010. **26**(11): p.
777 1449-1461.
- 778 33. Andersen, E.D., Roos, C., and Terlaky, T., On implementing a primal-dual interior-point
779 method for conic quadratic optimization. *Mathematical Programming*, 2003. **95**(2): p. 249-
780 277.
- 781 34. Oñate, E., Idelsohn, S.R., Del Pin, F., and Aubry, R., The Particle Finite Element Method - An
782 Overview. *International Journal of Computational Methods*, 2004. **01**(02): p. 267-307.
- 783 35. Edelsbrunner, H. and Mücke, E.P., Three-dimensional alpha shapes. *ACM Transaction on*
784 *Graphics*, 1994. **13**(1): p. 43-72.
- 785 36. Zhang, X., Krabbenhoft, K., Pedroso, D.M., Lyamin, A.V., Sheng, D., da Silva, M.V., and Wang,
786 D., Particle finite element analysis of large deformation and granular flow problems.
787 *Computers and Geotechnics*, 2013. **54**: p. 133-142.
- 788 37. Idelsohn, S., Mier-Torrecilla, M., and Oñate, E., Multi-fluid flows with the Particle Finite
789 Element Method. *Computer Methods in Applied Mechanics and Engineering*, 2009. **198**(33–
790 36): p. 2750-2767.
- 791 38. Cremonesi, M., Frangi, A., and Perego, U., A Lagrangian finite element approach for the
792 analysis of fluid–structure interaction problems. *International Journal for Numerical*
793 *Methods in Engineering*, 2010. **84**(5): p. 610-630.
- 794 39. Zhu, M. and Scott, M.H., Improved fractional step method for simulating fluid-structure

- 795 interaction using the PFEM. *International Journal for Numerical Methods in Engineering*,
796 2014. **99**(12): p. 925-944.
- 797 40. Zhang, X., Krabbenhoft, K., and Sheng, D., Particle finite element analysis of the granular
798 column collapse problem. *Granular Matter*, 2014. **16**(4): p. 609-619.
- 799 41. Zhang, X., Ding, Y., Sheng, D., Sloan, S.W., and Huang, W., Quasi-static collapse of two-
800 dimensional granular columns: insight from continuum modelling. *Granular Matter*, 2016.
801 **18**(3): p. 1-14.
- 802 42. Dávalos, C., Cante, J., Hernández, J.A., and Oliver, J., On the numerical modeling of granular
803 material flows via the Particle Finite Element Method (PFEM). *International Journal of Solids
804 and Structures*, 2015. **71**: p. 99-125.
- 805 43. Zhang, W., Yuan, W., and Dai, B., Smoothed Particle Finite-Element Method for Large-
806 Deformation Problems in Geomechanics. *International Journal of Geomechanics*, 2018. **18**(4):
807 p. 04018010.
- 808 44. Cremonesi, M., Ferrara, L., Frangi, A., and Perego, U., Simulation of the flow of fresh cement
809 suspensions by a Lagrangian finite element approach. *Journal of Non-Newtonian Fluid
810 Mechanics*, 2010. **165**(23–24): p. 1555-1563.
- 811 45. Monforte, L., Arroyo, M., Carbonell, J.M., and Gens, A., Numerical simulation of undrained
812 insertion problems in geotechnical engineering with the Particle Finite Element Method
813 (PFEM). *Computers and Geotechnics*, 2017. **82**: p. 144-156.
- 814 46. Zhang, X., Krabbenhoft, K., Pedroso, D., Lyamin, A., Sheng, D., Da Silva, M.V., and Wang, D.,
815 Particle finite element analysis of large deformation and granular flow problems. *Computers
816 and Geotechnics*, 2013. **54**: p. 133-142.
- 817 47. Zhang, X., Krabbenhoft, K., Sheng, D., and Li, W., Numerical simulation of a flow-like
818 landslide using the particle finite element method. *Computational Mechanics*, 2015. **55**(1): p.
819 167-177.
- 820 48. Cremonesi, M., Ferri, F., and Perego, U., A basal slip model for Lagrangian finite element
821 simulations of 3D landslides. *International Journal for Numerical and Analytical Methods in
822 Geomechanics*, 2017. **41**(1): p. 30-53.
- 823 49. Salazar, F., Irazábal, J., Larese, A., and Oñate, E., Numerical modelling of landslide-generated
824 waves with the particle finite element method (PFEM) and a non-Newtonian flow model.
825 *International Journal for Numerical and Analytical Methods in Geomechanics*, 2016. **40**(6): p.
826 809-826.
- 827 50. Shao, S. and Lo, E.Y.M., Incompressible SPH method for simulating Newtonian and non-
828 Newtonian flows with a free surface. *Advances in Water Resources*, 2003. **26**(7): p. 787-800.
- 829 51. Nomeritae, Daly, E., Grimaldi, S., and Bui, H.H., Explicit incompressible SPH algorithm for
830 free-surface flow modelling: A comparison with weakly compressible schemes. *Advances in
831 Water Resources*, 2016. **97**: p. 156-167.
- 832 52. Bird, R.B., Armstrong, R.C., and Hassager, O., *Dynamics of polymeric liquids* Vol. Fluid
833 Mechnics. 1987, New York: Wiley-Intersceience.
- 834 53. Bui, H.H., Fukagawa, R., Sako, K., and Ohno, S., Lagrangian meshfree particles method (SPH)
835 for large deformation and failure flows of geomaterial using elastic–plastic soil constitutive
836 model. *International Journal for Numerical and Analytical Methods in Geomechanics*, 2008.
837 **32**(12): p. 1537-1570.
- 838 54. Rzadkiewicz, S.A., Mariotti, C., and Heinrich, P., Numerical Simulation of Submarine
839 Landslides and Their Hydraulic Effects. *Journal of Waterway, Port, Coastal, and Ocean
840 Engineering*, 1997. **123**(4): p. 149-157.
- 841 55. Locat, A., Leroueil, S., Bernander, S., Demers, D., Jostad, H.P., and Ouehb, L., Progressive
842 failures in eastern Canadian and Scandinavian sensitive clays. *Canadian Geotechnical Journal*,
843 2011. **48**(11): p. 1696-1712.

844

845